Peer Community Journal

Section: Mathematical & Computational Biology

RESEARCH ARTICLE

Published
2023-07-21

Cite as
Sohrab Salehi, Fatemeh Dorri, Kevin Chern, Farhia Kabeer, Nicole Rusk, Tyler Funnell, Marc J. Williams, Daniel Lai, Mirela Andronescu, Kieran R. Campbell, Andrew McPherson, Samuel Aparicio, Andrew Roth, Sohrab P. Shah and Alexandre Bouchard-Côté (2023) *Cancer phylogenetic tree inference at scale from 1000s of single cell genomes* , Peer Community Journal, 3: e63.

Correspondence
bouchard@stat.ubc.ca

Peer-review
Peer reviewed and recommended by PCI Mathematical & Computational Biology, https://doi.org/10.24072/pci.mcb.100112

Cancer phylogenetic tree inference at scale from 1000s of single cell genomes

Sohrab Salehi[#,1], Fatemeh Dorri[#,2], Kevin Chern[3], Farhia Kabeer[,4], Nicole Rusk[,1], Tyler Funnell[,1], Marc J. Williams[,1], Daniel Lai[,4,5], Mirela Andronescu[4,5], Kieran R. Campbell[,6,7,8], Andrew McPherson[,1], Samuel Aparicio[,4,5], Andrew Roth[,2,4,5], Sohrab P. Shah[,1], and Alexandre Bouchard-Côté[3]

Volume **3** (2023), article e63

https://doi.org/10.24072/pcjournal.292

Abstract

A new generation of scalable single cell whole genome sequencing (scWGS) methods allows unprecedented high resolution measurement of the evolutionary dynamics of cancer cell populations. Phylogenetic reconstruction is central to identifying sub-populations and distinguishing the mutational processes that gave rise to them. Existing phylogenetic tree building models do not scale to the tens of thousands of high resolution genomes achievable with current scWGS methods. We constructed a phylogenetic model and associated Bayesian inference procedure, sitka, specifically for scWGS data. The method is based on a novel phylogenetic encoding of copy number (CN) data, the sitka transformation, that simplifies the site dependencies induced by rearrangements while still forming a sound foundation to phylogenetic inference. The sitka transformation allows us to design novel scalable Markov chain Monte Carlo (MCMC) algorithms. Moreover, we introduce a novel point mutation calling method that incorporates the CN data and the underlying phylogenetic tree to overcome the low per-cell coverage of scWGS. We demonstrate our method on three single cell datasets, including a novel PDX series, and analyse the topological properties of the inferred trees. Sitka is freely available at https://github.com/UBC-Stat-ML/sitkatree.git

[1]Computational Oncology, Department of Epidemiology and Biostatistics, Memorial Sloan Kettering Cancer Center, USA, [2]Department of Computer Science, University of British Columbia, Canada, [3]Department of Statistics, University of British Columbia, Canada, [4]Department of Pathology and Laboratory Medicine, University of British Columbia, Canada, [5]Department of Molecular Oncology, BC Cancer Research Centre, Canada, [6]Lunenfeld-Tanenbaum Research Institute, Mount Sinai Hospital, Canada, [7]Department of Molecular Genetics, University of Toronto, Canada, [8]Department of Statistical Sciences, University of Toronto, Canada, [#]Equal contribution

Contents

1. Introduction

A main challenge in investigating cancer evolution is the need to resolve the subpopulation structure of a heterogeneous tumour sample. Advances in next generation scWGS have enabled more accurate, quantitative measurements of tumours as they evolve (Baslan et al., 2012; Gawad et al., 2016; Laks et al., 2019; Pellegrino et al., 2018). Phylogenetic reconstruction is central to identifying clones in longitudinal xenoengraftment (Quinn et al., 2021; Salehi et al., 2021) as well as patients (Abbosh et al., 2017), and has been used to approximate the rate and timing of mutation (Wang et al., 2014) to determine the origins and clonality of metastasis (Leung et al., 2017; Yu et al., 2014).

Single cell cancer phylogenetics is an evolving field. Multiple approaches, spanning different study designs and data sources are reviewed in Schwartz and Schäffer, 2017. Many phylogenetic inference methods such as Scite, SciΦ, OncoNEM and SciClone use the often-made infinite site model assumption and consider point mutations as input or assume a small number of leaf nodes (Jahn et al., 2016; Miller et al., 2014; Ross and Markowetz, 2016; Singer et al., 2018). However, emerging single cell platforms produce up to thousands of single cell genomes and are suitable for determining copy number aberrations (CNA) (Laks et al., 2019; Zahn et al., 2017). Compared to phylogenetic methods based on point mutations, fewer can build phylogenies from large scale CN data. Recent related work includes MEDALT (Kaufmann et al., 2022), which models single-cell copy number lineages using a spanning tree over cells rather than a phylogeny; and SCARLET (Satas et al., 2020), which proposes a point mutation-based phylogeny inference procedure that calibrates mutation losses with copy number profiles. Distance based and agglomerative clustering methods such as neighbour joining (Wang et al., 2021; Xu et al., 2012) are often used to elucidate hierarchical structures over cells, in particular, in the context

of CNA, see Kaufmann et al., 2022, however, distance-based methods tend to produce less accurate tree reconstructions (Guindon and Gascuel, 2003; Kuhner and Felsenstein, 1994; Som, 2009; Williams and Moret, 2003).

Single cell whole genome DNA sequencing provides low, yet uniform coverage (Laks et al., 2019). That is, the sequenced reads cover for each single cell about 0.1 per cent of the genome. In this setting, most point mutations are not observed in most single cells making calling SNVs difficult. However, it is possible to identify the relative copy number for segments of the genome. These copy number events can be used as phylogenetic markers.

We describe sitka, a phylogenetic model and an associated Bayesian inference procedure designed specifically for inference based on CN information extracted from scWGS data (see Fig. 1). Our method addresses two key challenges: first, each CNA event typically affects a large number of genomic sites, breaking the independence assumptions required by existing phylogenetic methods (Ma et al., 2008; Malikic et al., 2019; Ross and Markowetz, 2016; Singer et al., 2018); second, while detailed modelling of dependent evolutionary processes is in principle possible, they entail computational requirements incompatible with the scale of modern scWGS data (Greenman et al., 2012). To confront these two difficulties, sitka uses a novel phylogenetic encoding of CN data, providing a statistical-computational trade-off by simplifying the site dependencies induced by rearrangements, while still forming a sound foundation to phylogenetic inference. Based on this encoding, we propose an innovative phylogenetic tree exploration move which makes the cost of Markov chain Monte Carlo (MCMC) iterations bounded by $O(|C|+|L|)$, where $|C|$ is the number of cells and $|L|$ is the number of loci. In contrast, existing off-the-shelf likelihood-based methods incur an iteration cost of $O(|C|\,|L|)$ (Ross and Markowetz, 2016; Singer et al., 2018; Zafar et al., 2017). Moreover, the novel move considers an exponential number of neighbouring trees whereas off-the-shelf moves consider a polynomial size set of neighbours.

Sitka's workflow proceeds by partitioning the CN information extracted from scWGS data of each cell into bins of fixed size (500Kb) with an integer CN state associated with each bin. This input data is then transformed into a binary format that captures CN changes, but not their direction or magnitude. Conditional on this binary encoding, sitka then yields an approximate posterior distribution on compatible phylogenetic trees.

Potential applications of sitka include lineage tracing and subclonal structure identification. In lineage tracing the goal is to relate single cells to their ancestors based on genomic markers. This is especially useful in experimental designs where multiple samples from the same subject exist, e.g., multi-region or timeseries studies (Salehi et al., 2021). In subclonal structure identification, the topology of the inferred phylogeny can be used to make inferences about the evolutionary forces acting on the trees (Househam et al., 2022).

We compare sitka with other tree inference methods on three real-world datasets, including triple negative breast cancer patient derived xenograft samples, high grade serous ovarian primary and matched relapse samples. Since the true phylogeny is unknown, we design a phylogenetic goodness-of-fit framework to quantitatively assess the performance of our method and to visualize reconstruction confidence as well as violations of our assumptions.

We use the sitka inferred trees to analyse the topological properties of the real-world datasets. Finally, we introduce a model extension that enables the placement of single nucleotide variants (SNV) with high levels of missingness on a tree inferred from the CN data.

2. Methods

2.1. Pre-processing

The raw data contain cells that are either contaminated (e.g., contains biological material from mice) or have undesired sequencing artefacts. These include cells that were captured for DNA sequencing when undergoing mitosis. Since the sitka model does not account for such phenomena, the filtering is an important step. Supplementary Fig. 1 shows the steps taken from pulling the raw data to the CNA integer matrix ready for sitka transformation (details in the Supplementary Information).

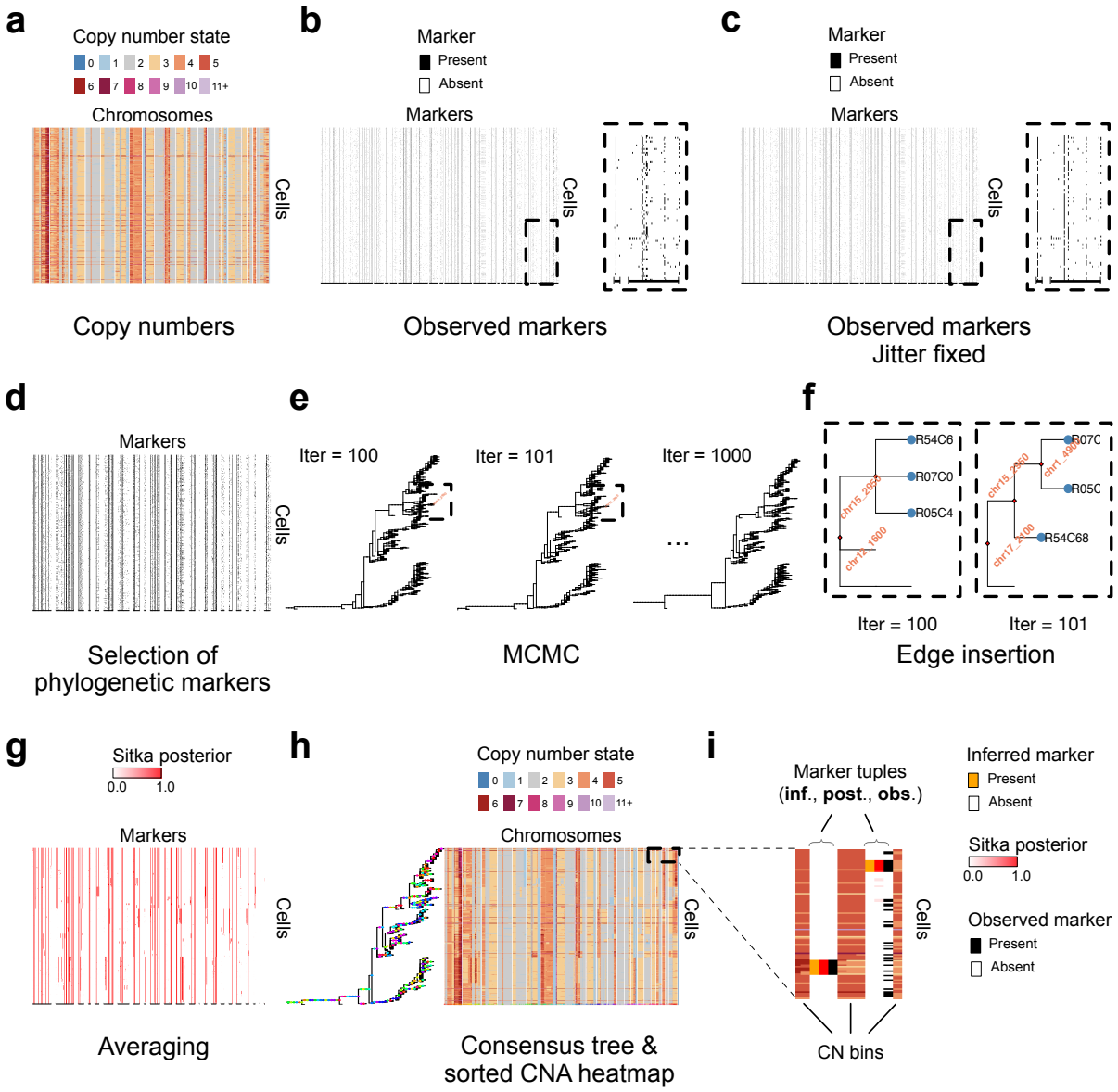

Figure 1 – (**a**) Sitka takes copy number calls data from a heterogeneous single-cell population. The cells (rows of the copy number matrix) are randomly sorted. (**b**) A lossy binary transformation is applied to obtain markers data. (Methods section 2.2 and Fig. 2). Note that each single-cell is now represented by the presence or absence of CN changes between consecutive bins. (**c**) The boundary conditions are smoothed to account for cell-specific marker misalignment (Methods section 2.3). Note how the columns in the inset in panel-**c** are less noisy than their counterpart in panel-**b**. (**d**) A subset of markers present in at least 5 percent of the cells are chosen for input to the tree inference algorithm. (**e**) An MCMC algorithm efficiently explores the tree space. (**f**) An example of an edge-insertion. The two insets are zoomed in from panel-**e**. Each inset depicts a subtree, where red diamonds and blue circles denote marker nodes and single-cells respectively. Also see Fig. 4 for details. (**g**) The indicator matrix of all post-burn-in MCMC trees are averaged to generate a matrix indicating the posterior probability of a cell being attached to a marker (Methods section 2.4.5). (**h**) The copy number data in (**a**) is sorted according to the inferred consensus tree, shown on the left of the matrix. (**i**) The inset shows the tuple of marker columns in the context of the copy number calls, namely **inf.** (inferred markers, i.e., latent state $x_{c,l}$), **post.** (posterior probability of the latent state $x_{c,l}$), and **obs.** (observed markers), interlaced with the CN columns (similar to Fig. 2). The results are from the *SA*535 dataset, a triple negative breast cancer patient derived xenograft sample (Methods section 3.2.)

Briefly, we remove control cells, cells with highly-noisy CN calls, and cells that have very few mapped reads. We also remove copy number bins that lie in difficult to sequence regions of the genome (bins with low-mappability). Finally, we drop cells that, based on their CNA profile, are suspected to be cycling cells. See the Section 1 of the supplementary text for further details.

2.2. The sitka transformation

To obtain the $C \times L_{\text{Markers}}$ phylogenetic markers matrix y that comprises the input to the sitka model, we apply a lossy transformation to the $C \times L_{\text{Bins}}$ CNA matrix a that involves computing the change in copy number state between two consecutive bins. Fig. 2 shows a small CNA matrix and its corresponding transformation into the marker matrix. For brevity, in what follows we assume that only one chromosome is used, so that $L_{\text{Bins}} = L$ and $L_{\text{Markers}} = L_{\text{Bins}} - 1$. In practice, we use all available chromosomes, and $L_{\text{Markers}} = L_{\text{Bins}} - N_{\text{Chr}}$ where N_{Chr} denotes the total number of chromosomes used.

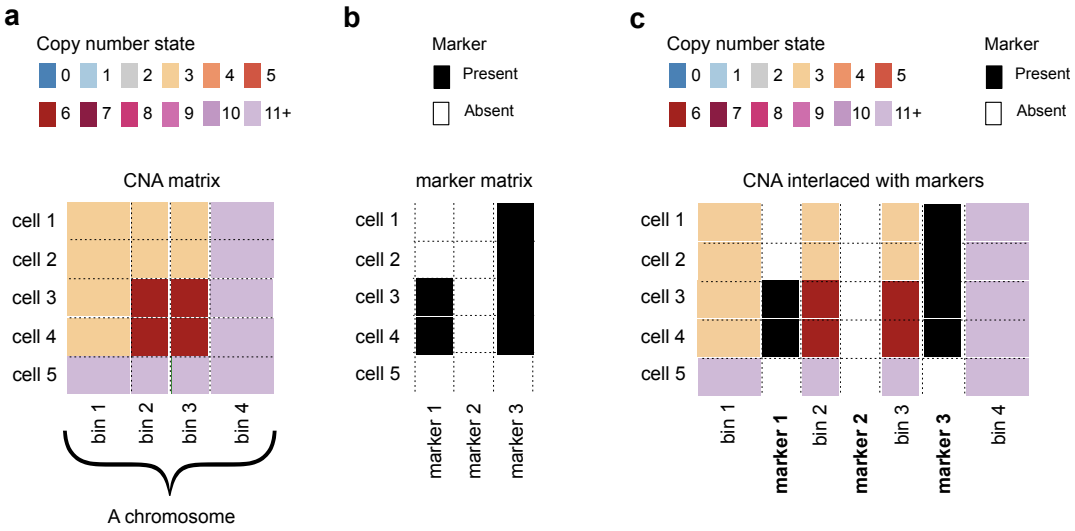

Figure 2 – A *bin* is a contiguous set of genomic positions. Each pair of consecutive bins (e.g., bins 1 and 2 in (**a**)) is associated with a *marker* (e.g., marker 1) that measures for each individual cell, whether there is a difference between the CNA states of the two bins. (**a**) The observed CNA matrix for a subset of bins on a chromosome. The rows are sequenced single cells, and the columns are bins. The CN states are colour-coded. (**b**) The three markers shown are associated with the four bins. Each marker records the presence (black) or absence (white) of a CN state change between a pair of consecutive bins. Note that in the CNA matrix, there is a CN change at row 3 from bin 1 to bin 2 (CN state 3 to 6). This is reflected in the marker matrix, at row 3 of marker 1 with a black square. There are no changes between bins 2 and 3 across any rows in the CNA matrix. This is reflected in marker 2 comprising all white squares. (**c**) For visualisation purposes, the CNA matrix can be interlaced with the marker matrix to more clearly show where the CNA changes occur. Each column of the marker matrix is inserted between the associated pair of columns in the CNA matrix. The resulting matrix is an example of an *augmented* view that combines data from two or more sources (here the CNA matrix and the marker matrix). In an augmented view, we call columns from each source a *channel*.

Given a filtered cell-by-locus matrix a, we sort bins by their genomic position. Then in each chromosome, we compute markers as the binarised difference between consecutive bins. In other words, $y = (y_{c,l'})$ and $l' \in \{1, \dots, L-1\}$, and

$$y_{c,l'} := \mathbf{1}\left(|a_{c,l'} - a_{c,l'+1}| > 0\right), \tag{1}$$

where $\mathbf{1}(x)$ is the indicator function.

2.3. Fixing jitter and selection of phylogenetic markers

The copy numbers available to us in this work are estimated independently for each cell. This is one reason why the start position (bin) of the same CN change event may be slightly different across cells, generating some *jitter*. We address this by enumerating each change point column in order of decreasing density (where the density of column l is given by $\sum_{c \in C} y_{c,l}/|C|$) and merging the column with its $k = 2$ immediate neighbours (see Algorithm 1 for details). An example of the result of the jitter correction heuristic is shown in Fig. 1 panel **c**. To speed-up computation, only a subset of markers present in at least a minimum number of cells are chosen for phylogenetic inference. That is, we removed columns l in y with relative density $\sum_{c \in C} y_{c,l}/|C|$ less than a threshold, set to 5%. Larger values of this threshold may lead to less resolved clades in the inferred tree.

Algorithm 1 JitterFix

```
procedure jitter-fix(y, k)
    column-queue ← OrderByDensityDecreasing(y)
    columns-visited ← {}
    for column-index c in column-queue do
        neighbours ← neighbours (c, y, k)
        for column-index n in neighbours do    ▷ The function neighbours is defined as the k columns to the left and k to the right of c (when applicable)
            if n ∉ columns-visited then
                y_{1:C,c} ← y_{1:C,c} ∨ y_{1:C,n}
                y_{1:C,n} ← 0
                columns-visited ← columns-visited ∪ n
    return y
```

2.4. The sitka model

2.4.1. Model description. The sitka model starts with the perfect phylogeny assumption for the latent variables $x_{c,l}$ but allows deviation from it via allowing noisy observations $y_{c,l}$. In a perfect phylogeny model, each phylogenetic trait arises only once on the rooted tree topology and all cells descending from that position will inherit that trait and no deletions are allowed.

Let C and L denote the sets of cells and loci respectively.

We posit an observation probability model $p(y|x, \theta)$, where θ are model parameters described shortly, and both x and y are cell by locus matrices, the former being latent (derived from the unobserved tree via $x = x(t)$), while the latter is the matrix obtained from the sitka transformation. To model errors in copy number calls as well as perfect phylogeny violations, we introduce false positive and negative rate parameters $r^{\text{FP}} \in (0, 1)$ and $r^{\text{FN}} \in (0, 1)$ respectively, and an error matrix

$$e^{r^{\text{FP}}, r^{\text{FN}}} = \begin{bmatrix} 1 - r^{\text{FP}} & r^{\text{FP}} \\ r^{\text{FN}} & 1 - r^{\text{FN}} \end{bmatrix},$$

$$p\left(y_{c,l} | x_{c,l}, r^{\text{FP}}, r^{\text{FN}}\right) = e^{r^{\text{FP}}, r^{\text{FN}}}_{x_{c,l}, y_{c,l}},$$

from which we set:

$$p(y|x, \theta) = \prod_{l \in L} \prod_{c \in C} p\left(y_{c,l} | x_{c,l}, r^{\text{FP}}_{c,l}(\theta), r^{\text{FN}}_{c,l}(\theta)\right).$$

We define two type of models, differing in the choice of functions $r^{\cdot}_{c,l}(\cdot)$ and dimensionality of θ: one based on global error parameters, and one based on locus-specific error parameters.

For the global parameterization, $\theta = \theta_{\text{global}} = (r^{\text{FN}}_{\text{global}}, r^{\text{FN}}_{\text{global}})$, and the false positive and false negative functions are given by $r^{\text{FP}}_{c,l}(\theta_{\text{global}}) = r^{\text{FP}}_{\text{global}}$ and $r^{\text{FN}}_{c,l}(\theta_{\text{global}}) = r^{\text{FN}}_{\text{global}}$.

For the locus-specific error model, we set the error rates to be locus-dependent: $\theta = (r^{\text{FP}}_1, r^{\text{FP}}_2, \ldots, r^{\text{FP}}_{|L|}, r^{\text{FN}}_1, r^{\text{FN}}_2, \ldots, r^{\text{FN}}_{|L|})$, $r^{\text{FP}}_{c,l}(\theta) = r^{\text{FP}}_l$ and $r^{\text{FN}}_{c,l}(\theta) = r^{\text{FN}}_l$. With this extra flexibility, the model can discount the effect of a trait violating the perfect phylogeny assumption, by setting high error rates for the trait's locus.

The two parameterizations are compared in the Supplementary Information. We use the global parameterization by default unless mentioned otherwise.

In both the global and locus-specific parameterizations, we need to construct a prior distribution $p(\theta)$ over the error parameters. Using a uniform prior distribution with support on $[0, 1]$ can lead to pathological cases as shown in Fig. 3. To avoid that, we use the following prior distributions on the two types of error:

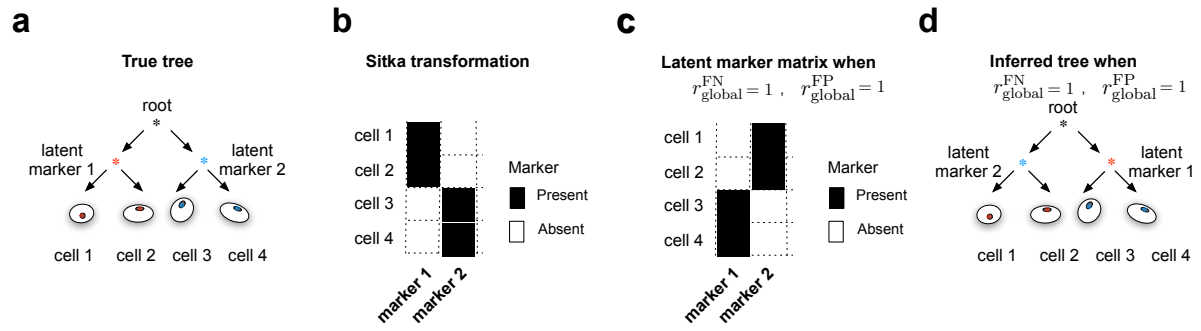

Figure 3 – (**a**) The true tree reconstruction in a simple example with a balanced phylogeny with two clades of size two, and two unique markers, coloured red and blue, that distinguish the left and right clades respectively. (**b**) The binarised input matrix corresponding to the four cells at the two markers. The desired observation error rates should be zero and the latent and observed marker matrices should match exactly, as the perfect phylogeny assumption holds. If the observation error parameters are set to one, that is $r^{FP}_{global} = 1$ and $r^{FN}_{global} = 1$, then the latent marker matrix with all entries flipped as shown in (**c**) will have an equal likelihood under this setting as the desired latent matrix has when error rates are set to zero. (**d**) The incorrect tree reconstruction where the left and right clades are erroneously assigned to the blue and red markers.

$$r^{FP} \sim \text{Uniform}\left(0, \overline{r^{FP}}\right),$$
$$r^{FN} \sim \text{Uniform}\left(0, \overline{r^{FN}}\right).$$

We use $\overline{r^{FP}} = 1/2$ and $\overline{r^{FN}} = 1/2$ in our experiments involving synthetic data. For experiments on real world data, we use $\overline{r^{FP}} = 1/10$ and $\overline{r^{FN}} = 1/2$ as default. When the model is misspecified from an overly conservative bound, the trace, and thus posterior distribution, collapses to the boundaries. For example, when using a false positive rate of 0.1 for synthetic data, the resulting approximate marginal posterior of the false positive rate corresponds to a near-point mass at 0.1. We did not observe such boundary collapse on the real datasets studied in this work.

Next, we describe the prior $p(t)$ on phylogenies using a two-step generative process:

Sampling a mutation tree:: let $\mathcal{V}^m = L \cup \{v^*\}$ denote a vertex set composed of one vertex for each of the $|L|$ loci plus one artificial root node v^*. The artificial root node induces an implicit notion of direction on the edges, viewing them as pointing away from v^*. Let $\mathcal{T}^m$ denote the set of trees t^m spanning $\mathcal{V}^m$. The interpretation of t^m is as follows: there is a directed path from vertex/locus l to l' in t^m if and only if the trait indexed by l is hypothesized to have emerged in a cell which is ancestral to the cell in which l' emerged. Pick one element $t^m \in \mathcal{T}^m$.

Sampling cell assignments:: assign each cell to a vertex in t^m. The interpretation of assigning cell c to locus l is that among the traits under study, c is hypothesized to possess only the traits visited by the shortest path from v^* to l in t_m. If a cell c is assigned to v^*, the interpretation is that c is hypothesized to possess none of the traits under study.

The number of possible trees obtained from this two-step sampling process is:

$$\begin{aligned}|\mathcal{T}| &= |\mathcal{T}^{\mathrm{m}}||\{f : C \to L \cup \{v^*\}\}| \\ &= (|L|+1)^{(|L|+1)-2}(|L|+1)^{|C|} \\ &= (|L|+1)^{|L|+|C|-1},\end{aligned}$$

where we use Cayley's formula to compute $|\mathcal{T}^{\mathrm{m}}|$. Hence the uniform prior probability mass function over the possible outputs of this two-step sampling process is given by:

$$p(t) = \frac{\mathbf{1}[t \in \mathcal{T}]}{(|L|+1)^{|L|+|C|-1}},$$

where $\mathcal{T}$ is the set of all perfect phylogenetic trees that result from the two step generative process described above. Simulation from the prior can be performed using Wilson's algorithm (Wilson, 1996), followed by independent categorical sampling to simulate the cell assignments.

This simple prior has a useful property: if a collection of say two splits are supported by m_1 and m_2 traits, then the prior probability for an additional trait to support the first versus second split is proportional to (m_1+1, m_2+1). Therefore, there is a "rich gets richer" behaviour built-in into the prior, which is viewed as useful in many Bayesian non-parametric models (Teh et al., 2010). More precisely, this "rich gets richer" behaviour emerges when grouping trees into equivalence classes and looking at the induced prior on these equivalence classes, i.e., the distribution obtained by summing the prior over the trees in the equivalence class. Specifically, consider the equivalence relation such that two type I trees t, t' are in the same equivalence class if and only if $f(t) = f(t')$, where $f(\cdot)$ consists in transforming t into a type II tree while annotating each edge by the number of events on that edge. Since there are different numbers of type I trees in different equivalent classes, this means that the induced prior on these equivalence classes is non-uniform.

2.4.2. Inference. The posterior distribution,

$$\pi(t, \theta) \propto p(t)p(\theta)p(y|x(t), \theta),$$

is approximated using MCMC. Two MCMC moves are used, described in the next two sections. The posterior distribution is summarized using a Bayes estimator described in Section 2.4.5. The model is implemented in the Blang probabilistic programming language (Bouchard-Côté et al., 2022).

2.4.3. MCMC tree exploration move. Sitka uses a tree sampling move to efficiently explore, at each MCMC iteration, the posterior distribution in a large neighbourhood of a given tree. Given a tree t and locus l, we define a neighbourhood $N^l(t) \subset \mathcal{T}$ by removing l from t, and considering all possible ways to reattach l and hence defining a neighbourhood of phylogenetic trees (we also implemented a separate move reattaching cell nodes instead of locus nodes, its derivation follows similar lines as the move described in this section). The process of removing l is called an *edge-contraction* (removing an edge after connecting its two end-points) while the process of adding back a locus is called an *edge-insertion*. An edge insertion (see Fig. 4 for a visualization) can be described as follows:

(1) Pick a non-cell vertex v, i.e., an element from the set $R = \{v^*\} \cup L \backslash \{l\}$ where v^* is the root node.
(2) Pick any subset of v's descendent subtrees and disconnect them from v.
(3) Add a new node l under v and move the selected nodes from step 2 above and attach them to l.

In the following, we derive the probability distributions to be used in steps 1 and 2 above that lead to a Gibbs sampling algorithm (Geman and Geman, 1984). The Gibbs sampler first selects a locus l from a fixed distribution (a tuning parameter), which we take for simplicity as being uniform over the $|L|$ loci.

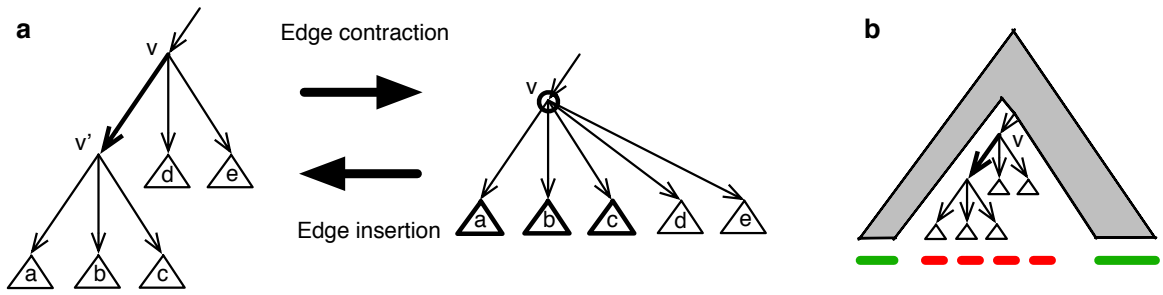

Figure 4 – (**a**) Reading from left to right: the interpretation of removing a column in the matrix x is to perform contraction of an edge corresponding to a locus shown in bold. Reading from right to left: the interpretation of inserting back a column while assigning new binary values is an edge insertion. The circled node v refers to Step 1. The subtrees in bold refer to those selected in Step 2. The edge in bold, the one introduced in Step 3. (**b**) Decomposition used for the recursion of Section 2.4.3.

After having sampled l, we partition $N^l(t_{\setminus l})$ into blocks corresponding to the choice of node v made in Step 1, $N^l(t_{\setminus l}) = \cup_v N^l_v(t_{\setminus l})$. The Gibbs conditional probabilities required in step 1 above are of the form:

$$\bar{\rho}_v = \frac{\rho_v}{\sum_{\tilde{v}\in R}\rho_{\tilde{v}}},$$

where:

$$\rho_v = \sum_{t\in N^l_v(t_{\setminus l})} p(t)p(y|x(t),\theta), \tag{2}$$

and $t_{\setminus l}$ denotes the tree obtained after performing an edge contraction, where the contracted edge is between l and the parent node of l. To compute ρ_v efficiently, we start with the following likelihood recursion for all vertex v in $t_{\setminus l}$. First, for all vertices c corresponding to a cell and $b \in \{0,1\}$, define:

$$p^b_c = p\left(y_{c,l}|b,\theta\right).$$

Next, we perform the following bottom-up recursion for all subtrees of $t_{\setminus l}$: for all $v \in R$, $b \in \{0,1\}$,

$$p^b_v = \prod_{v''\in \text{children}(v)} p^b_{v''},$$

where children(v) denotes the list of children of vertex v.

We can now return to the problem of computing $\bar{\rho}_v$. First, observe that the sum in Equation (2) can be re-indexed by a bit vector $\mathbf{b} = (b_1, b_2, \ldots, b_k)$, $b_{v''} \in \{0,1\}$ of length equal to $k = |\text{children}(v)|$. Each bit $b_{v''}$ is equal to one if children v'' is to be moved into a child of v' (refer to Fig. 4), and zero if it is to stay as a child of v. For each possible assignment, we obtain a tree $t \in N^l_v(t_{\setminus l})$, and its probability can be decomposed into factors corresponding to cells that are descendant of v (denoted C_v, solid red thick line under the tree of Fig. 4-**B**) and those that are not (denoted $C_{\setminus v}$, dashed green thick line under the tree of Fig. 4-**B**).

The product of the likelihood factors corresponding to cells that are not descendants of v ("outside product") does not depend on the choice of the bit vector. This outside product can be obtained as follows:

$$\prod_{c\in C_{\setminus v}} p^0_c = \frac{p^0_{v^*}}{p^0_v}.$$

Note that this assumes $p^0_v > 0$. As a workaround to cases where there are structural zeros, we recommend injecting small numerical values if $p^0_v = 0$ (we used 10^{-6} in our implementation).

For the cells under v, we now have to take into account whether they are selected under the newly introduced locus or not. More precisely, for each of the children $v_1, v_2, \dots, v_k$, we have to take into account the value of the bit vector $b = (b_1, b_2, \dots, b_k)$. The sum over possible assignments written naively has a number of terms which is exponential in k, but can be rewritten into a product over k factors:

$$\sum_{t \in N_v^l(t_{\setminus l})} \prod_{c \in C_v} p_c^{x_{c,l}(t)} = \sum_{b_1=0}^{1} \dots \sum_{b_k=0}^{1} \prod_{i=1}^{k} p_{v_i}^{b_i} = \prod_{i=1}^{k} (p_{v_i}^0 + p_{v_i}^1).$$

Putting it all together, we obtain for some constants K_i independent of v:

$$\begin{aligned}
\rho_v &= K_1 \sum_{t \in N_v^l(t_{\setminus l})} p(y|x(t), \theta) \\
&= K_1 \sum_{t \in N_v^l(t_{\setminus l})} \prod_{l' \in L} \prod_{c \in C} p\left(y_{c,l'} | x_{c,l'}(t), r_{c,l'}^{\mathrm{FP}}(\theta), r_{c,l'}^{\mathrm{FN}}(\theta)\right) \\
&= K_1 \left(\prod_{l' \in L, l' \neq l} \prod_{c \in C} p\left(y_{c,l'} | x_{c,l'}(t), r_{c,l'}^{\mathrm{FP}}(\theta), r_{c,l'}^{\mathrm{FN}}(\theta)\right) \right) \sum_{t \in N_v^l(t_{\setminus l})} \prod_{c \in C} p\left(y_{c,l} | x_{c,l}(t), r_{c,l}^{\mathrm{FP}}(\theta), r_{c,l}^{\mathrm{FN}}(\theta)\right) \\
&= K_1 K_2 \sum_{t \in N_v^l(t_{\setminus l})} \prod_{c \in C} p\left(y_{c,l} | x_{c,l}(t), r_{c,l}^{\mathrm{FP}}(\theta), r_{c,l}^{\mathrm{FN}}(\theta)\right) \\
&= K_1 K_2 \sum_{t \in N_v^l(t_{\setminus l})} \prod_{c \in C} p_c^{x_{c,l}(t)} \\
&= K_1 K_2 \sum_{t \in N_v^l(t_{\setminus l})} \left(\prod_{c \in C_v} p_c^{x_{c,l}(t)} \right) \left(\prod_{c \in C_{\setminus v}} p_c^{x_{c,l}(t)} \right) \\
&= K_1 K_2 \left(\prod_{c \in C_{\setminus v}} p_c^{x_{c,l}(t)} \right) \sum_{t \in N_v^l(t_{\setminus l})} \prod_{c \in C_v} p_c^{x_{c,l}(t)} \\
&= K_1 K_2 \left(\frac{p_{v^*}^0}{p_v^0} \right) \sum_{t \in N_v^l(t_{\setminus l})} \prod_{c \in C_v} p_c^{x_{c,l}(t)} \\
&= K_1 K_2 \left(\frac{p_{v^*}^0}{p_v^0} \right) \prod_{i=1}^{k} (p_{v_i}^0 + p_{v_i}^1) \\
&= K_1 K_2 K_3 \frac{\prod_{i=1}^{k} (p_{v_i}^0 + p_{v_i}^1)}{p_v^0}.
\end{aligned}$$

Putting these together we can compute the probabilities required in step 1 above:

$$\bar{\rho}_v = \frac{\rho_v}{\sum_{\tilde{v} \in R} \rho_{\tilde{v}}} \tag{3}$$

$$= \frac{\left(\frac{\prod_{v_i \in \mathrm{children}(v)} \left(p_{v_i}^0 + p_{v_i}^1\right)}{p_v^0} \right)}{\sum_{\tilde{v} \in R} \left(\frac{\prod_{v_i' \in \mathrm{children}(\tilde{v})} \left(p_{v_i'}^0 + p_{v_i'}^1\right)}{p_{\tilde{v}}^0} \right)}. \tag{4}$$

Once v is sampled, we choose a subset of its children to move to v' by sampling k independent Bernoulli random variables with the i-th one having bias

$$\frac{p_{v_i}^1}{p_{v_i}^0 + p_{v_i}^1},$$

and selecting children with corresponding Bernoulli realisations of 1.

2.4.4. MCMC parameter exploration move. To resample the parameters θ we condition on the tree t, and hence on the hidden state matrix x, and update θ in a Metropolis-within-Gibbs framework. There are two different samplers depending on whether the global or locus-specific parameterization is used. We start with describing the former.

We compute two sufficient statistics from the matrix x (i) the number of false positive instances, n^{FP}, and (ii) the number of false negative instances, n^{FN},

$$n^{\mathrm{FP}} = n^{\mathrm{FP}}(x) = \sum_{c \in C} \sum_{l \in L} \mathbf{1}[x_{c,l} = 0, y_{c,l} = 1]$$
$$n^{\mathrm{FN}} = n^{\mathrm{FN}}(x) = \sum_{c \in C} \sum_{l \in L} \mathbf{1}[x_{c,l} = 1, y_{c,l} = 0].$$

Based on these cached statistics, we obtain:

$$p(y|x, \theta_{\mathrm{global}}) \propto \left(r^{\mathrm{FP}}\right)^{n^{\mathrm{FP}}} \left(r^{\mathrm{FN}}\right)^{n^{\mathrm{FN}}} \left(1 - r^{\mathrm{FP}}\right)^{n^{\mathrm{N}} - n^{\mathrm{FN}}} \left(1 - r^{\mathrm{FN}}\right)^{n^{\mathrm{P}} - n^{\mathrm{FP}}}, \tag{5}$$

where the the number of positive n^{P} and negative n^{N} instances in the data can be pre-computed,

$$n^{\mathrm{P}} = \sum_{c \in C} \sum_{l \in L} \mathbf{1}[y_{c,l} = 1]$$
$$n^{\mathrm{N}} = |C||L| - n^{\mathrm{P}}.$$

Based on the above expression, which can be evaluated in $O(1)$ once the statistics are computed, we then use a slice sampling algorithm to update the parameters (Neal, 2003).

The sampler for the locus-specific parameterization is very similar. The main difference is that we compute the statistics for each locus l:

$$n_l^{\mathrm{FP}} = n_l^{\mathrm{FP}}(x) = \sum_{c \in C} \mathbf{1}[x_{c,l} = 0, y_{c,l} = 1]$$
$$n_l^{\mathrm{FN}} = n_l^{\mathrm{FN}}(x) = \sum_{c \in C} \mathbf{1}[x_{c,l} = 1, y_{c,l} = 0]$$
$$n_l^{\mathrm{P}} = \sum_{c \in C} \mathbf{1}[y_{c,l} = 1]$$
$$n_l^{\mathrm{N}} = |C| - n_l^{\mathrm{P}}$$
$$p(y|x, \theta) = \prod_l \left(r_l^{\mathrm{FP}}\right)^{n_l^{\mathrm{FP}}} \left(r_l^{\mathrm{FN}}\right)^{n_l^{\mathrm{FN}}} \left(1 - r_l^{\mathrm{FP}}\right)^{n_l^{\mathrm{N}} - n_l^{\mathrm{FN}}} \left(1 - r_l^{\mathrm{FN}}\right)^{n_l^{\mathrm{P}} - n_l^{\mathrm{FP}}}.$$

Then a slice sampling move is applied to each locus-specific parameter.

2.4.5. Posterior summarization. To summarize the posterior distribution using a point estimate, we approximate the Bayes estimator (Robert, 2007) by minimising the Bayes risk for a loss function $\tilde{L}(a, (t', \theta'))$ encoding the cost of selecting an "action" a when the true tree is t' and the true parameter is θ':

$$\arg\min_a \sum_{t' \in \mathcal{T}} \int \tilde{L}(a, (t', \theta')) \pi(t', \theta') \, \mathrm{d}\theta'. \tag{6}$$

Here, an "action" consists in selecting a consensus tree t. Moreover, the loss function we consider only depends on the true tree t' and not on the true parameter θ', so we write this loss function as $L(t, t')$, simplifying the above equation into:

$$\tau_{\mathrm{Consensus}} = \arg\min_{t \in \mathcal{T}} \sum_{t' \in \mathcal{T}} \int L(t, t') \pi(t', \theta') \, \mathrm{d}\theta'. \tag{7}$$

One default choice for $L(t, t')$ is the L_1 metric on the matrices of induced indicators $x(t), x(t')$:

$$L(t, t') = \sum_{l \in L} \sum_{c \in C} |x_{c,l}(t) - x_{c,l}(t')|.$$

It is useful to define the marginal indicators $m_{c,l}$ that can be conceptualised as the posterior probability of cell c to have trait l:

$$m_{c,l} = \sum_{t' \in \mathcal{T}} \int \mathbf{1}[x_{c,l}(t') = 1] \pi(t', \theta') \, \mathrm{d}\theta'.$$

Using the MCMC samples $t^1, t^2, \ldots, t^N$, we obtain a Monte Carlo approximation:

$$\bar{m}_{c,l} = \frac{1}{N} \sum_{i=1}^{N} x_{c,l}(t^i) \to m_{c,l},$$

with probability one.

Fig. 1-**g** shows an example of the matrix m each element of which is one of the approximated $\bar{m}_{c,l}$. We can now write the objective function of Equation (7) via the above marginal indicators:

$$\begin{aligned}
\sum_{t' \in \mathcal{T}} \int L(t, t') \pi(t', \theta') \, \mathrm{d}\theta' &= \sum_{t' \in \mathcal{T}} \int \sum_{l \in L} \sum_{c \in C} |x_{c,l}(t) - x_{c,l}(t')| \pi(t', \theta') \, \mathrm{d}\theta' \\
&= \sum_{l \in L} \sum_{c \in C} \sum_{t' \in \mathcal{T}} \int |x_{c,l}(t) - x_{c,l}(t')| \pi(t', \theta') \, \mathrm{d}\theta' \\
&= \sum_{l \in L} \sum_{c \in C} \{ m_{c,l}(1 - x_{c,l}(t)) + (1 - m_{c,l}) x_{c,l}(t) \} \\
&= \sum_{l \in L} \sum_{c \in C} \{ x_{c,l}(t) - 2 m_{c,l} x_{c,l}(t) \} + \text{constant}. \qquad (8)
\end{aligned}$$

We use a greedy algorithm to approximately minimize Equation (8). We start with a star tree with leaves C rooted at v^* and add loci from L one by one from a locus queue sorted by priority score. The priority score of each locus l is computed as

$$\text{priority}(l) = \max_{t' \in N^l(t)} \frac{q(t')}{\sum_{t'' \in N^l(t)} q(t'')},$$

where

$$q(x) = \prod_{c \in C} \prod_{l \in L(x)} q_{c,l}(x_{c,l})$$
$$q_{c,l}(x_{c,l}) = 2 m_{c,l} x_{c,l} - x_{c,l}.$$

The quantities in the priority queue can be computed as in Section 2.4.3. We take the result of the minimization of the Bayes risk as the consensus tree $\tau_{\text{Consensus}}$.

2.4.6. Consensus tree and CNA heatmap visualisation. To visualize the consensus tree, we collapse the chains (sequence of loci having only one child) as well as remove the subtrees containing no cells. We align the leaves of the tree which correspond to cells after collapsing to the rows of a cell-locus matrix.

2.5. Synthetic experiments

2.5.1. Benchmarking. To assess the performance of sitka against alternative approaches, we ran inference on 90 simulated datasets of varying characteristics. We will refer to this set of datasets as $S90$; its simulation procedure is described in Section 2.5.3. Fig. 5 shows four such simulated datasets. For each dataset in $S90$, we scored each method by computing the Robinson-Foulds (RF) (Robinson and Foulds, 1981) distance between the simulated tree and the inferred tree. The scores were normalized within each dataset by dividing each method's score by the worst performing method's score (note that the set of methods includes sampling a tree uniformly at random; the motivation of this normalization is to correct for the intrinsic difficulty of datasets).

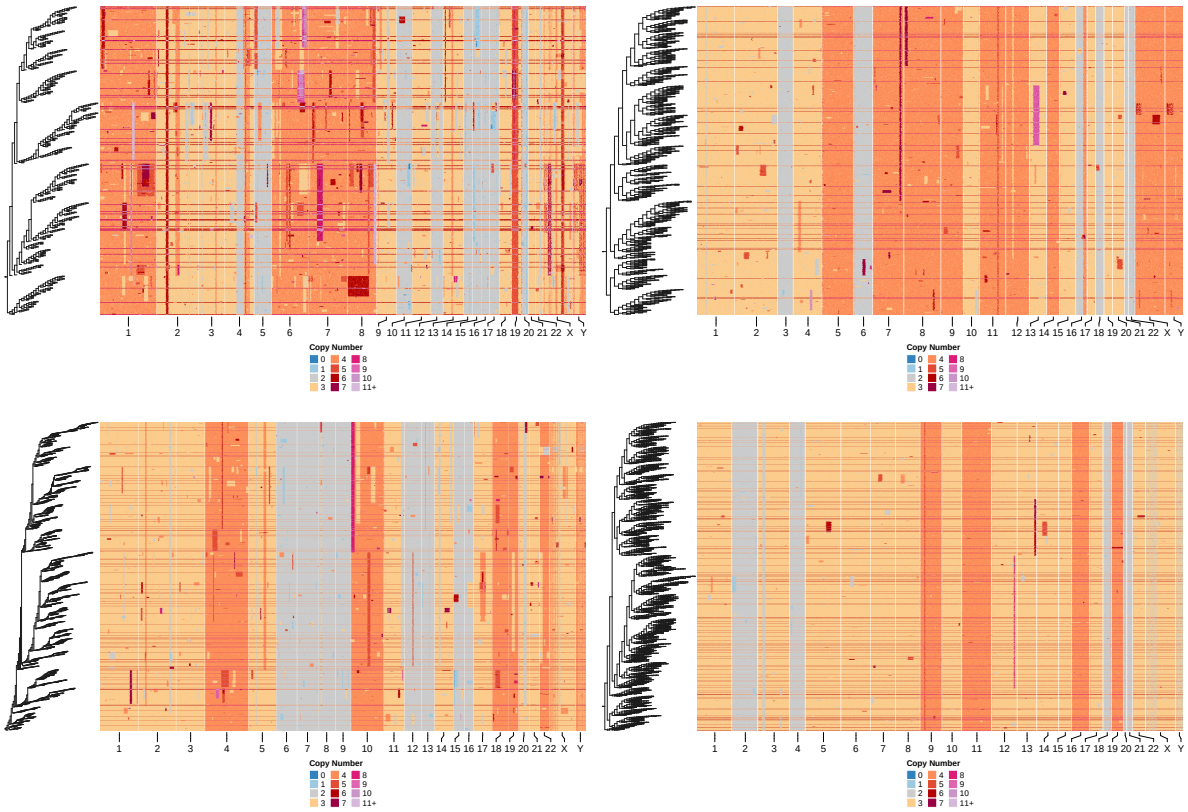

Figure 5 – Synthetic datasets simulated from the GBFBS model. The number of cells, number of loci, and β values are are $(500 \times 800, -0.83)$, $(1000 \times 400, -0.1)$, $(2000 \times 800, -0.9)$, $(3000 \times 400, -0.48)$ for the upper left, upper right, lower left, and lower right figures respectively.

We compared sitka against the following baseline methods: `UPGMA`, `WPGMA`, `NJ`, `HDBSCAN`, and balanced and ordinary least-squares minimum-evolution methods (`BME`, `OME` respectively) of Desper and Gascuel, 2002. We also report the score of a uniformly random bifurcating tree, `Uniform`, to help interpret the absolute scores. Each method was given raw data from $S90$, as well as input identical to that of sitka, i.e., filtered binary marker data. Sitka's inference settings are summarized in Supplementary Table 1.

Baseline methods performed significantly worse with sitka's input and are thus omitted from the following summary. Sitka's normalized RF score (0.57 ± 0.04) outperformed all baseline methods, the next best performer was `BME` (0.91 ± 0.07). Sitka ranked first in all 90 but one set of data, where it ranked third for one dataset of size 500×800. These results are summarized in Fig. 6.

2.5.2. Exploratory experiments within sitka. To explore the effectiveness of global versus *local* (locus-specific) parameterization (Section 2.4.1), and the posterior summarization method (Section 2.4.5), we ran inference on 10 synthetic datasets. We will refer to this set of datasets as $S10$; its simulation procedure is described in Section 2.5.3. Inference settings are summarized in Supplementary Table 1.

RF distances from the *best-possible tree* were computed as a metric. The best-possible tree is defined as the perfect phylogenetic tree constructed from the noiseless synthetic, unviolated cell-locus matrix data. Note that the best possible tree is derived from the *true tree* (i.e., the one used in the first step of the generating process), but in general can be different. To understand why, note that the tree generation process will simulate on each edge of the true tree a Poisson distributed number of evolutionary events (Section 2.5.3). As a result, some edges can have zero associated evolutionary events. This means that even if we turned off all observation noise it would not be possible to recover these zero-event edges, they are in a sense unidentifiable. The

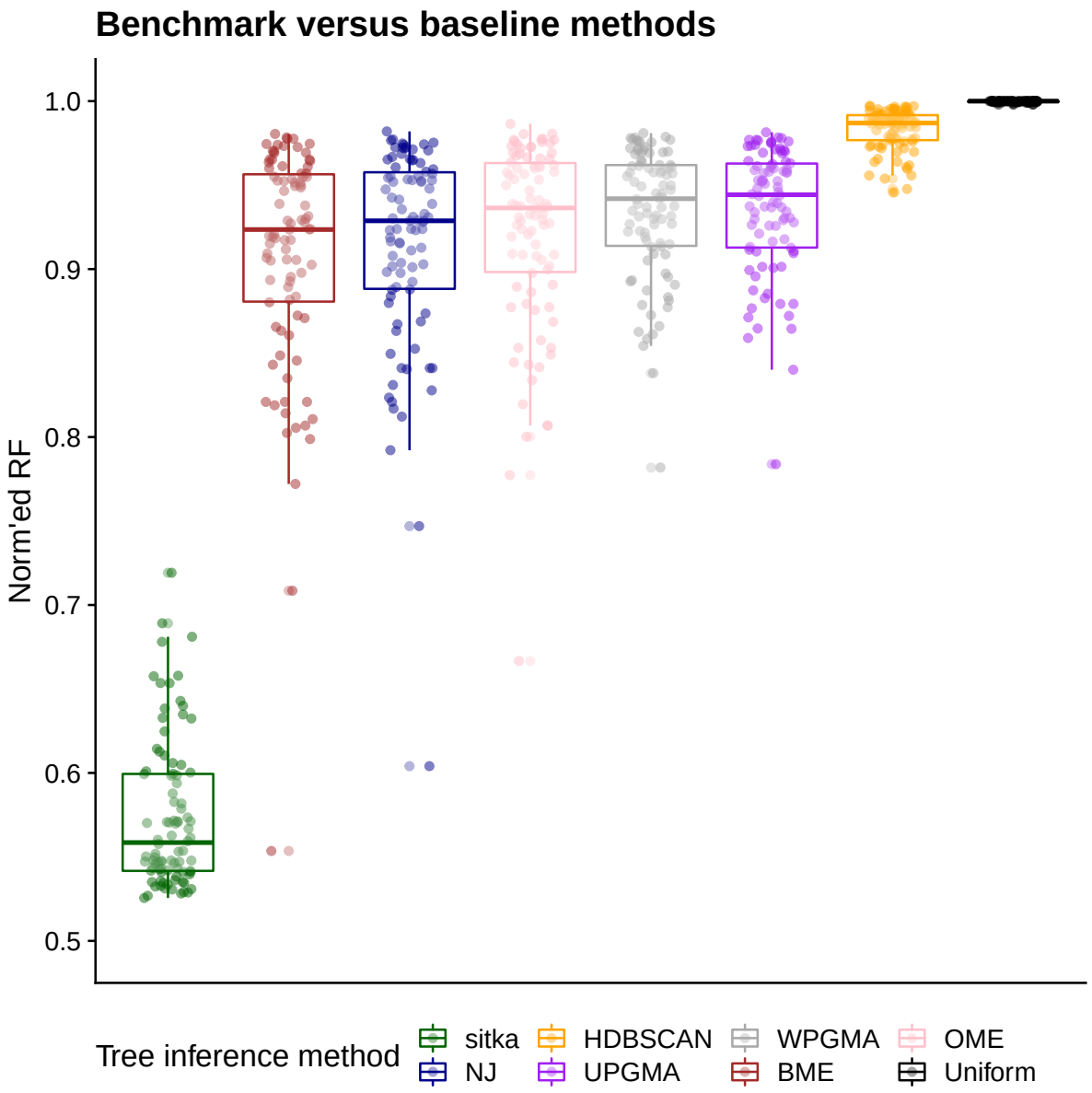

Figure 6 – Tree reconstruction evaluation using a normalized Robinson–Foulds metric on synthetic datasets from *S*90, simulated from Beta-splitting processes. Here normalization is done by dividing the RF distance of each inference method by the worst performer per dataset.

process of producing the best possible tree essentially consists in collapsing these zero-event edges, hence forming a multifurcating reference tree.

For a baseline with which to compare the greedy estimator (GE) of Section 2.4.5, consider the *trace search estimator* (TSE). The TSE is defined as a tree in the sampler trace that minimizes the sample L_1 distance (Section 2.4.5). Formally,

$$\tau_{\text{TSE}} = \underset{t \in \{t^i\}}{\arg\min} \sum_{t' \in \{t^i\}} L(t, t'),$$

where $\{t^i\}$ denotes the set of trees that were sampled during the MCMC procedure.

The GE method outperformed the TSE method under both the global and local models. This suggests the proposed GE can, informally, harness more information from the posterior. Under the TSE, the global model (0.44 ± 0.09; mean normalized RF score $\pm$ standard error) outperformed the local model (0.71 ± 0.06). This observation suggests that the local parameterization has a

strong influence on the trace (in tree space) of our sampler, as the TSE is essentially a search over the posterior sample. Under the GE, the global model (0.31 ± 0.07) and local model (0.30 ± 0.07) performed evenly well. This observation suggests that the choice of parameterization does not heavily influence the information contained in the marginal posterior over trees. Ultimately this experiment suggests that the GE summarizes the marginal posterior sufficiently well such that the global model, the simpler model of the two, suffices for reconstructing phylogenies and should be the preferred model. A summarizing plot is shown in Fig. 7.

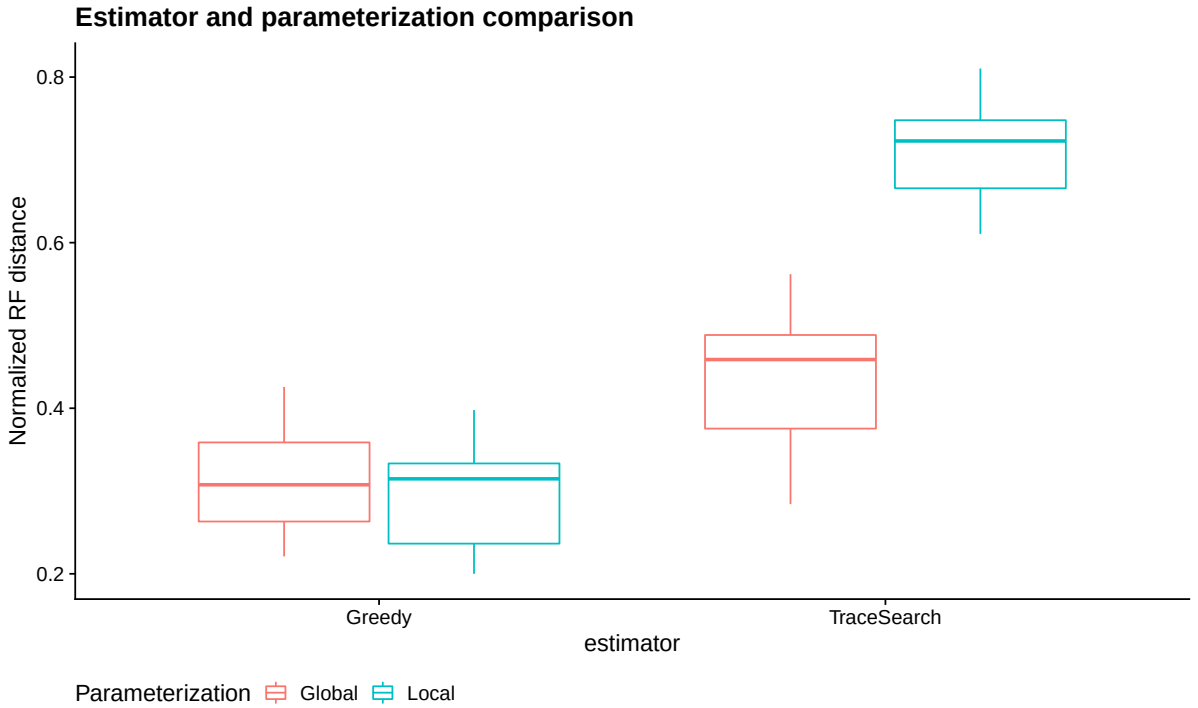

Figure 7 – A model and estimator comparison based on tree reconstruction accuracy for datasets from $S10$. For each dataset, inference was performed on both the globally- and locally-parameterized model. Both the greedy and trace search estimates were computed for each inference result.

In our next synthetic experiment, we aimed to study the effects of perfect phylogeny assumption violations on the reconstruction of trees, and attempted to draw connections to real world data. The two violations considered are infinite sites and loss violations, described in Section 2.5.3. Inference was performed on 130 datasets ($S130$). Inference settings are summarized in Supplementary Table 1, and the simulation procedure for $S130$ is described in Section 2.5.3.

The experiment results are summarized in Fig. 8-**a**. Holding one violation rate fixed at zero and varying the other, we observed linear effects for both types of violations. The results suggest sitka is more robust to infinite sites violations, with estimated effects to be 0.31 ± 0.07 (normalized RF distance $\pm$ standard error), which is much less than loss violations (0.47 ± 0.07). When varied together, the linear effects were estimated to be $0.25 \pm 0.04, 0.38 \pm 0.04$ respectively. In an attempt to draw connections to real datasets, we developed a heuristic method to obtain a rough estimate of both violation rates. The estimated rates obtained on real data were all less than 0.25 (the estimation heuristic is described below; Fig. 8-**b**).

We now describe the heuristic we used to obtain rough estimates of the rates of the two types of violation. Given the inferred tree and its corresponding marker matrix x (as in Section 2.4.1), and the sitka-transformed marker matrix y (as in Section 2.2), define the difference matrix $z := x - y$, i.e., z has entries $z_{i,j} = x_{i,j}(t) - y_{i,j}$, where t is the consensus reconstruction. To motivate how we can detect violations of the Infinite Site assumption (IS, i.e., genomic bins in which more than one events occur), and losses, refer to Fig. 9, and notice that these violations tend to leave a distinctive pattern on the difference of the two matrices x (positive entries shown

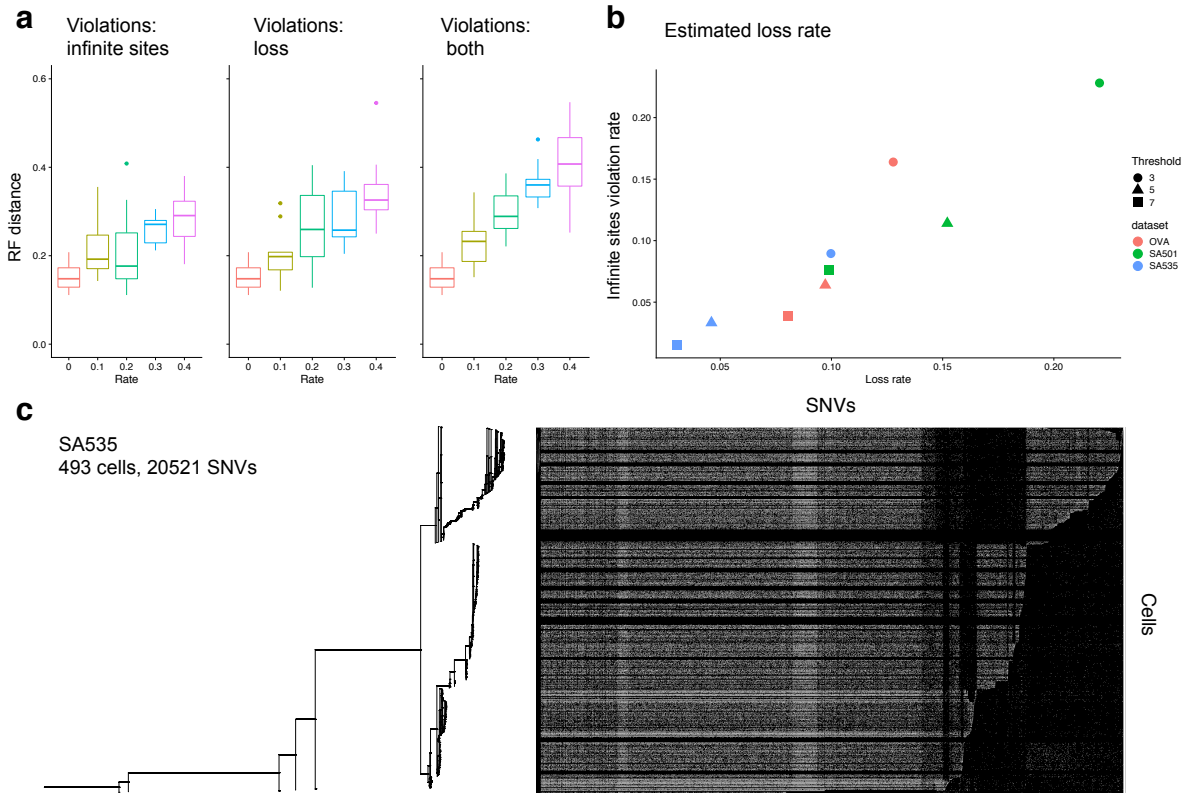

Figure 8 – (**a**) RF distance of sitka tree estimate to the best-possible tree. The first plot holds p_{is} constant at zero. The second plot holds p_{loss} constant at 0. The third plot varies $p_{is} = p_{loss}$ jointly. **(b)** Estimation of violation rates in real data and a set of synthetic data. (**c**) Over 20,000 SNV's with high levels of missingness are placed on a backbone tree inferred from the CNA data for *SA*535.

in black in the Figure) and y (positive entries shown in orange in the Figure). Specifically, define z_{Loss} with entries $z^{\text{Loss}}_{i,j} := \mathbf{1}(z_{i,j} > 0)$, and similarly z_{IS} with entries $z^{\text{IS}}_{i,j} := \mathbf{1}(z_{i,j} < 0)$. Given an integer-valued threshold $\epsilon_v > 0$, we say a column or trait l in z_v (for $v \in \{\text{Loss}, \text{IS}\}$) has a violation if there exists an *island* of size at least as large as ϵ_v. An island of size s in column l is defined to be any sequence of row indices $i, i+1, \ldots, i+s$ such that $z^v_{i,l} = z^v_{i+1,l} = \cdots = z^v_{i+s,l} = 1$ and $z^v_{i-1,l}, z^v_{i+s+1,l}$ are, not necessarily the same, 0 or undefined. Finally, the proportion of columns with a given type of violation, loss or infinite sites, is taken to be the violation rate estimate.

We also performed experiments to compare our full Bayesian analysis to Maximum Likelihood estimation (MLE). To do so, we generated data as follows: we first sampled a tree generated uniformly over topologies; second, we generated synthetic data according to $y_{c,l}|x_{c,l} \sim \text{Normal}(x_{c,l}, \sigma^2)$, varying σ^2 to control the amount of noise. We generate matrices of size $|C| = 1000$ and $|L| = 50$ for $\sigma^2 \in \{1/10, 2/10, \ldots, 5/10\}$. In these experiments we provide the well-specified noise model to both inference methods. We approximate the MLE using a greedy scheme with the same structure as the one described in Section 2.4.5. The results are shown in Fig. 10. The Bayesian methods outperform the greedy maximum likelihood heuristic by a large margin.

Finally, we investigate the impact of ignoring pairwise dependencies between the two end points of CNA events. We first make the observation that if we subset the sitka markers to keep only those where the copy number is increasing from left to right, we retain only one end point of each paired event. This creates a smaller set of independent markers $L' \subset L$. We can compute one sitka tree t based on all L loci (which includes ignored pairwise dependencies), and one sitka tree t' based on L' (a smaller set of independent loci). We can then inspect the proportion of identical entries in the matrices $x(t')$ compared to $x(t)$, the latter subsetted to the columns in L'.

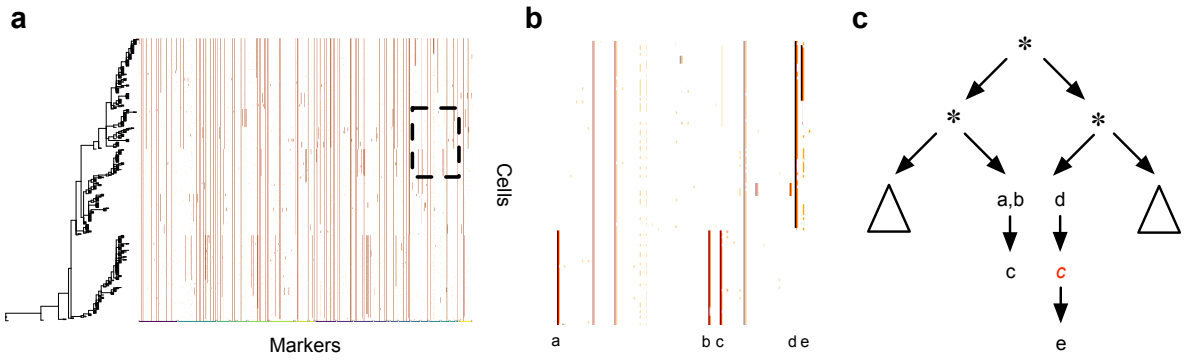

Figure 9 – A locus in *SA*535 that violates the perfect phylogeny assumption. The method is robust to this violation and correctly allocates the other relations (positive x entries shown in black in the matrix; positive y entries shown in orange; posterior marginals m in shades of red). **(a)** the part of the tree where the violation occurs, magnified in **(b)**, where the short band of orange not matched with a black band is indicative of the violation. **(c)** the corresponding tree showing the two points of the tree where the two events collocated in the same bin occurred in the tree. The sister clades of a,b and d suggest that this is a case of two insertion events rather than a loss.

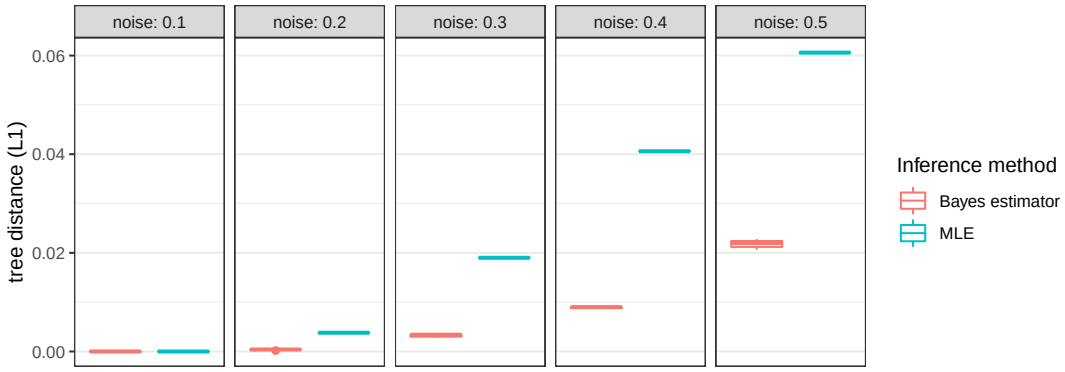

Figure 10 – Synthetic data results comparing our Bayesian estimator to a Maximum Likelihood Estimator (MLE). Boxes from left to right show different amounts of noise in the synthetic data generation, corresponding to values for σ^2. The y axis measures the L1 tree distances loss, normalized by $|C||L|$.

We performed the experiment described above on the S90 datasets (described in 2.5.3) with three noise regimes described as follows: (I) where step (ii) in 2.5.3 is skipped; (II) uniform noise parameters FPR and FNR drawn from uniform distributions on the intervals $(0.0005, 0.005)$, $(0.005, 0.015)$ respectively, doubling noise parameters drawn from a uniform distribution on $(0.015, 0.035)$ distribution, jitter noise parameters drawn from a uniform distribution on $(0.15, 0.35)$; (III) uniform noise parameters FPR and FNR drawn from uniform distributions on the intervals $(0.001, 0.01)$, $(0.01, 0.03)$ respectively, doubling noise parameters drawn from a uniform distribution on $(0.03, 0.07)$ distribution, jitter noise parameters drawn from a uniform distribution on $(0.3, 0.7)$. All results are averaged over 15 datasets.

In all three noise regimes we observed a large overlap between t and t', but this overlap is negatively correlated with noise: in regime (I) we observed a mean overlap of 0.99 (sd 0.004); in regime (II), a mean overlap of 0.97 (sd 0.009); in regime (III), a mean overlap of 0.76 (sd 0.18). The results support that in a low to moderate noise regime, it is reasonable to ignore violation of pairwise dependencies for the purpose of point estimation (consensus tree construction). In the higher noise regime, it may be advantageous to build the two trees t and t'. We expect neither to systematically outperform the other, the trade-off being that t is built from more data

but with independence violations, whereas t' is built from less data but without independence assumption violations. Our goodness-of-fit tests can be used to select one of these two trees for final output.

2.5.3. Data simulation. Datasets in $S90$ were generated in two steps: (i) simulate a cell tree and its corresponding CNA data, and (ii) inject noise into the CNA data from step one.

In the first step we used the simulator of Mallory et al., 2020 to generate trees along with CNAs, where leaf nodes represent observed cells and internal nodes represent latent ancestral cells, i.e., unobserved cells. An edge in the tree represents an ancestral relationship between the respective cells.

The simulator of Mallory et al., 2020 itself consists of two parts, which we briefly describe as follows. First, the simulator samples a tree based on a generalization of the Blum-François Beta-splitting (GBFBS) model (Blum and François, 2006; Sainudiin and Véber, 2016), which is inspired by the Beta-splitting model of Aldous, 1996. Authors of Sainudiin and Véber, 2016 argue the GBFBS model is capable of realizing topologies comparable to that of the original Beta-splitting model. When $\beta = \alpha \to -1$, trees are totally imbalanced; when $\beta = \alpha \to \infty$, trees are perfectly balanced. The Beta-splitting model is particularly well-suited for generating a wide range of topologies, varying from balanced to imbalanced tree structures. Second, given a tree, CNAs are simulated on the edges of the tree where the number and size of CNAs are drawn from Poisson and exponential distributions respectively. The simulator also accounts for clonal whole chromosome amplification events, motivated by punctuated evolution models (Gao et al., 2016).

The second step of our synthetic data simulation process, independent of Mallory et al., 2020, injects noise into a cell by locus input CNA matrix y, and outputs a noisy matrix of the same size. Three types of noise were employed, namely, uniform noise, jitter noise, and a doubling noise.

The uniform noise is parameterized by false positive (FPR) and false negative (FNR) rate parameters. For each element of the input matrix y_{ij}, add an integer $N_{ij} \sim \text{Binomial}(y_{ij}, \text{FNR})$ or subtract an integer $M_{ij} \sim \text{Binomial}(1, \text{FPR})$.

The doubling noise is parameterized by a probability p_d: for each row of the CNA matrix y, draw a factor K where $K - 1 \sim \text{Binomial}(1, p_\text{d})$, which is then multiplied to the row of the CNA matrix as noise. This procedure effectively, on average, doubles the copy number values for p_d proportion of cells in the sample.

The jitter noise is parameterized by a probability p_j. First, map the CNA matrix to its marker matrix. Then for each marker, the locus corresponding to the marker is randomly duplicated to the previous bin(s), or the next bin(s). The number of bins J to be overwritten — zero, one, or two — is drawn from a Binomial$(2, p_\text{j})$ distribution.

Datasets in $S90$ were of sizes $\{500, 1000, 1500, 2000, 2500, 3000\}$ cells by (approximately) $\{400, 600, 800\}$ markers. For each combination of sizes, we generated five datasets based on different random seeds and parameters to make a total of $6 \times 3 \times 5 = 90$ datasets. The approximate number of markers is the target number of markers after correcting for jitter and filtering. Fig. 5 shows the CNA profiles of a subset of simulated data.

To describe the simulation parameters used for $S90$, we follow the terminologies and notation used in Mallory et al., 2020. For generating trees, the α and β values parameterize the generalized Beta-splitting model. We used a symmetric parameterization of $\alpha = \beta \in \{-0.9, -0.83, -0.7, -0.48, -0.1\}$. For generating CNA data, the mean number of CNA to be added to a branch in the tree was chosen to generate data with approximately the number of desired markers post filtering and jitter-fixing. The multiplier of the mean CNA on the root was set to 8, the whole amplification rate (rate of an allele chosen to be amplified) was set to 0.5. The remaining parameters used default settings. See Mallory et al., 2020 for a more thorough description of parameters.

For injecting noise, we drew the uniform noise parameters FPR and FNR from uniform distributions on the intervals $(0.001, 0.01)$, $(0.01, 0.03)$ respectively. The doubling noise parameters p_d were drawn from a Uniform$(0.03, 0.07)$ distribution. The jitter noise parameters p_j were drawn from a Uniform$(0.3, 0.7)$ distribution.

Datasets in $S10$ and $S130$ were also generated in two steps: (i) simulate a cell tree and its corresponding binary marker data satisfying perfect phylogeny assumptions, and (ii) inject noise and/or violations into the the binary marker data from step one.

In the first step, a tree is generated via Kingman's coalescent (Kingman, 1982). We used the R packages (Schliep, 2011; Staab and Metzler, 2016) for simulation. Briefly, we sample a coalescent tree for the set of cells C by uniformly selecting pairs of cells $c_i, c_j \in C$ to coalesce backwards in time. The waiting time, or the branch length, between each event is exponentially distributed. Conditionally on the coalescent tree and given a set of loci L, we simulate a $|C| \times |L|$ marker matrix y. Every entry $y_{i,j}$ is initialized to 0. Then for each column l, we select a subset of cells C' from C to set $y_{i,l}$ to 1, for all $i \in C'$. The subset of cells is sampled by choosing a branch on the tree with probability proportional to the branch length, and selecting all cells descendant from the selected branch. In essence, we are simulating the number of events via a Poisson process, and directly mapping these events to the cell-locus marker matrix. The above concludes the data generation procedure satisfying perfect phylogeny assumptions.

In the second step of $S10$'s simulator, we injected artificial noise by introducing standard false positive and negative values into y. This concludes $S10$'s simulator. The simulator for $S130$ has an additional sampling step for controlling the degree of perfect phylogeny violations. We considered two types of violations: (i) the loss of markers along a tree's branches, and (ii) the violation of the infinite sites (IS) assumption, that is, the occurrence of multiple distinct events in the same locus.

The procedure for simulating loss of marker events can be described as follows. First, randomly select a locus l, then identify the most recent common ancestor a for the set of cells $\{i : y_{i,l} = 1\}$. Given a, sample a cell d descendant of a (including a). Finally, the loss event is simulated by reverting $y_{i,l}$ to 0, for all i descendant of, and including, d.

IS model violations were simulated as follows. Uniformly sample a pair of loci (j, k), and merge $y_{\cdot,j}, y_{\cdot,k}$ into one column, yielding a cell-locus matrix of size one less than the original size. However, to maintain control over $|L|$, datasets in $S130$ were simulated with $|L| + N_{\text{IS}}$ loci such that after simulating IS violations, we recover a matrix of size $|C| \times |L|$, where N_{IS} is the number of IS violations.

The total number of loss and infinite sites violation events (N_{Loss}, N_{IS}) were drawn from binomial distributions with probability $p_{\text{Loss}}, p_{\text{IS}}$ respectively (and size $|L|$). As a final step, false positives and negatives were artificially injected.

For both $S10$ and $S130$, datasets of size $|C| \times |L| = 500 \times 100$ with FNR and FPR both set to 0.002 were generated. For $S130$, the unordered pair $(p_{\text{Loss}}, p_{\text{IS}})$ were set to values in $\{(0, 0), (0.1, 0.1), \ldots, (0.4, 0.4)\} \cup \{(0, 0.1), (0, 0.2), (0, 0.3), (0, 0.4)\}$. For each configuration of simulation parameters, 10 different seeds were used to generate a total of 10 and 130 datasets for $S10$ and $S130$ respectively.

2.6. Goodness-of-fit

To evaluate the goodness-of-fit of inferred trees on real data, we suggest a test comparing the posterior distribution over entries of the matrix x with the data y.

Since we will assess the goodness-of-fit of not only our method but also different baseline, we start by explaining how we can generalize the notion of the x matrix used in our method to other tree reconstruction methods. To do so, consider an inferred rooted tree, τ, and define a matrix-value function $g(\tau)$ as follows. If τ is a tree inferred from sitka, set $g(\tau) = x(\tau)$. For trees inferred from baseline methods, we proceed as follows. Let τ denote a rooted tree, u, one of its unlabelled internal nodes, and c one of its leaves. Let clade(u) denote the clade corresponding to u, i.e., the set of leaves descendent from u. We define $g_{c,u}(\tau) = \mathbf{1}[c \in \text{clade}(\tau)]$.

In general the inferred trees from the baseline methods do not have named internal nodes, nor do they have the same number of internal nodes as the number of loci L. Therefore we do not know which locus in the inferred tree τ corresponds to which locus in the matrix y. We note that this is not the case with trees inferred from sitka where the internal nodes of the tree correspond to the columns of the induced genotype matrix g. As a result, for methods other

than sitka, for each column in the input data matrix, we pick a clade in τ that has the highest prediction accuracy for the entries in that column.

More precisely, for each method, we report Youden's J index (Youden, 1950) which is equal to the sum of the sensitivity and specificity minus 1. We now define a binary classification counts matrix function h, i.e., a function which, for two vectors w and z of length C, forms the confusion matrix:

$$h_{i,j}(w,z) = \sum_{c \in C} \mathbf{1}\left(w_c = i\right) \mathbf{1}\left(z_c = j\right).$$

For example $h_{0,0}(w,z)$ would count the number of times both elements of w and z were equal to zero (or *true negative*). We define accuracy for a given confusion matrix $h = h(w,z)$ as

$$\text{acc}(h) := \frac{h_{0,0} + h_{1,1}}{\sum_{i,j} h_{i,j}}.$$

We further define sensitivity and specificity as

$$\begin{aligned}
\text{sensitivity}(h) &:= \frac{h_{1,1}}{h_{1,1} + h_{1,0}}, \\
\text{specificity}(h) &:= \frac{h_{0,0}}{h_{0,0} + h_{0,1}}, \\
\text{youden}(h) &:= \text{sensitivity}(h) + \text{specificity}(h) - 1.
\end{aligned}$$

For a given tree τ and its corresponding genotype matrix $g = g(\tau)$ we compute the Youden's score as follows:

(1) for all locus l in y, $h_l := \arg\max_{l' \in \text{columns}(g)} \text{acc}\left(h(y_l, g_{\cdot,l'})\right)$,
(2) $h_\tau := \sum_{l' \in \text{columns}(g)} h_{l'}$
(3) $\text{youden}_\tau := \text{youden}(h_\tau)$.

That is for each locus in y, we take the clade that among all possible clades in τ maximizes the accuracy in predicting which cells are present in the l-th column of y. We then sum over all these scores to compute a confusion matrix for τ and use this agglomerative matrix to compute the Youden's score for the tree. We use the delta method to calculate confidence intervals. Recall that the delta method is concerned with the asymptotic behaviour of a distribution for a function ψ of an asymptotically Gaussian random vector. For a sequence of random vectors X_n for which $\sqrt{n}(X_n - \theta) \xrightarrow{D} \mathcal{N}(0, \Sigma)$, we have that $\sqrt{n}(\psi(X_n) - \psi(\theta)) \xrightarrow{D} \mathcal{N}(0, \nabla\psi \cdot \Sigma \cdot \nabla\psi)$. In this context we use the identity

$$\text{youden}(h) = \frac{\frac{1}{|C|} h_{1,1}}{\frac{1}{|C|} h_{1,1} + \frac{1}{|C|} h_{1,0}} + \frac{\frac{1}{|C|} h_{0,0}}{\frac{1}{|C|} h_{0,0} + \frac{1}{|C|} h_{0,1}} - 1 =: \psi\left(\frac{1}{|C|} h_{0,0}, \frac{1}{|C|} h_{0,1}, \frac{1}{|C|} h_{1,0}, \frac{1}{|C|} h_{1,1}\right).$$

Fig. 11-**d** shows the Youden's score and its 95% confidence interval for sitka and 6 baseline methods on 3 different real-world datasets. Sitka has a higher score than all competing methods.

2.7. Application: assignment of single nucleotide variants

Here we posit an observation probability model for adding single nucleotide variant (SNV) data to an existing phylogenetic tree.

For locus l in cell c, let $y^{SNV}_{c,l} = (d_{c,l}, \nu_{c,l}, c_{c,l})$ denote the observed SNV data where the total number of reads, the number of reads with a variant allele, and the corresponding copy number are indicated by $d_{c,l}$, $\nu_{c,l}$, and $c_{c,l}$ respectively.

We use $x^{SNV}_{c,l}$ to denote an indicator variable taking the value one if and only if an ancestor of cell c harboured a single nucleotide alteration event at locus l. This variable is unobserved and the focus of inference in this section. As in the sitka model, we assume a perfect phylogeny structure on these indicator variables, and add an error model to relate $x^{SNV}_{c,l}$ to the observed data while allowing violations of the perfect phylogeny assumption and measurement noise. In the context of single nucleotide data, this is similar to (Jahn et al., 2016). The parameters of the

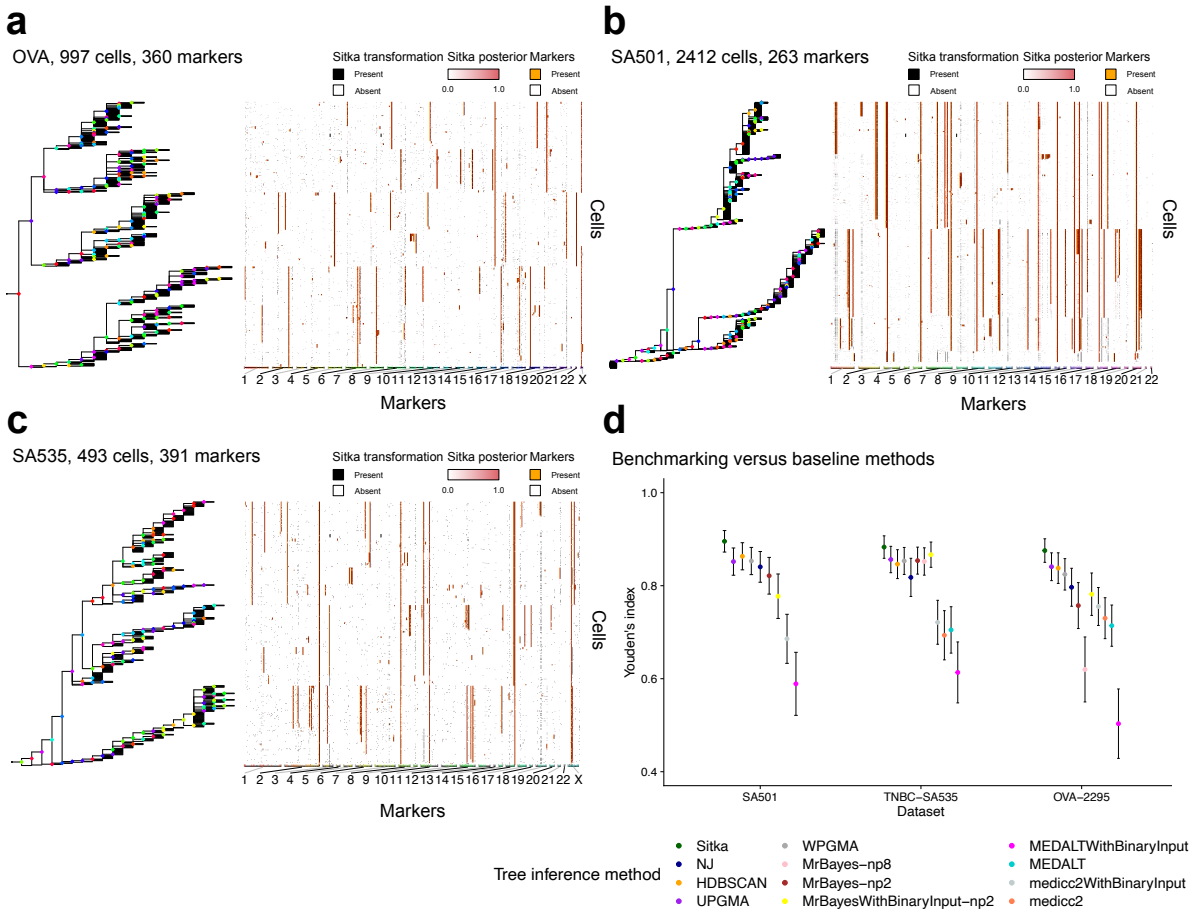

Figure 11 – (**a**), (**b**), and (**c**) show the consensus tree and marker-space matrix for the *OVA*, *SA*501, and *SA*535 datasets respectively. (**d**) Comparison to baseline methods.)

error model are denoted $\theta^{SNV} = (\epsilon_{FP}, \epsilon_{FN})$, where ϵ_{FP} and ϵ_{FN} are false positive rate and false negative rates, respectively. Define:

$$q^b_{c,l} = p(y^{SNV}_{c,l} | x^{SNV}_{c,l}, \theta^{SNV}) = p(\nu_{c,l} | d_{c,l}, c_{c,l}, x^{SNV}_{c,l} = b, \theta^{SNV}), \tag{9}$$

where $d_{c,l}$ and $c_{c,l}$ are given inputs. The likelihood probability of cell node c is denoted by $q^b_{c,l}$, where $b \in \{0, 1\}$. For $b = 1$, $q^b_{c,l}$ reflects the likelihood of cell c being mutated at locus l; and for $b = 0$, $q^b_{c,l}$ reflects the likelihood of cell c not being mutated at locus l. For $d_{c,l} = 0$, we set $q^b_{c,l} = 0.5$.

The probability $q^b_{c,l}$ is obtained by marginalizing a mixture of binomial distributions depending on all possible genotype states of locus l at cell c. Given the copy number $c_{c,l}$, the possible genotype states are $\mathcal{G} = \{A \dots A, AA \dots B, A \dots BB, \dots, B \dots B\}$, where each element has a length equal to $c_{c,l}$. For example, the genotype AAB refers to a genotype with one variant allele B and two reference alleles A. For each genotype state g_i, where i indexes the elements of $\mathcal{G}$, the mean parameter of the corresponding binomial distribution is denoted by $\xi^i_{c,l}$:

$$\xi^i_{c,l} = \begin{cases} \frac{\mathcal{B}(g_i)}{c_{c,l}}, & 1 \leq \mathcal{B}(g_i) < c_{c,l}, \\ 1 - \epsilon_{FP}, & \mathcal{B}(g_i) = c_{c,l}, \\ \epsilon_{FP}, & \text{otherwise}, \end{cases} \tag{10}$$

where $\mathcal{B}(g_i)$ represents the number of variant alleles of genotype g_i. Therefore, for $b = 1$,

$$q^1_{c,l} = p(\nu_{c,l}|d_{c,l}, c_{c,l}, x^{SNV}_{c,l} = 1, \theta^{SNV}) \tag{11}$$

$$= \sum_{i=1}^{c_{c,l}} p(g_i)[\xi_{c,l}^{\nu_{c,l}}(1-\xi_{c,l})^{d_{c,l}-\nu_{c,l}}] + \epsilon_{FN}[\epsilon_{FP}^{\nu_{c,l}}(1-\epsilon_{FP})^{d_{c,l}-\nu_{c,l}}]. \tag{12}$$

The value of $p(g_i)$ equals $\frac{1-\epsilon_{FN}}{c_{c,l}}$, and ϵ_{FN} represents the error due to mutation loss or tree errors.

If the mutation status of cell c at locus l is a wildtype (i.e., mutation is not present), then the possible genotype states should not have any variant allele. The only possible genotype state is $\{A \dots A\}$. The mean parameter of the binomial distribution equals ϵ_{FP} (false positive rate). Therefore,

$$q^0_{c,l} = p(\nu_{c,l}|d_{c,l}, c_{c,l}, x^{SNV}_{c,l} = 0, \epsilon_{FP}). \tag{13}$$

With the proposed probability model for SNVs, we can incorporate both SNV data and CNA data to infer the underlying tree phylogeny in the sitka model. Therefore,

$$p(y|x,\theta) = \prod_{c\in C}\prod_{l\in L_{CNA}} p(y^{CNA}_{c,l}|x^{CNA}_{c,l}, \theta^{CNA}) \prod_{l\in L_{SNV}} p(y^{SNV}_{c,l}|x^{SNV}_{c,l}, \theta^{SNV}), \tag{14}$$

where C and L are the disjoint set of cells and loci, respectively. In this section, the loci set L includes both CNA and SNV traits.

Assume now that we seek to add one locus to an existing tree. We proceed similarly to Section 2.4.3. Equation (4) can be rewritten in the following form:

$$\bar{\rho}_v = \frac{\left(\frac{\prod_{v_i\in \text{children}(v)}(\gamma^0_{v_i}+\gamma^1_{v_i})}{\gamma^0_v}\right)}{\sum_{\bar{v}\in R}\left(\frac{\prod_{\bar{v}_i\in \text{children}(\bar{v})}(\gamma^0_{\bar{v}_i}+\gamma^1_{\bar{v}_i})}{\gamma^0_{\bar{v}}}\right)}, \tag{15}$$

where γ^b_v, for $b \in \{0,1\}$ is:

$$\gamma^b_v = \begin{cases} p^b_v, & \text{if } l \text{ represents a CNA locus,} \\ q^b_v, & \text{if } l \text{ represents a SNV locus.} \end{cases}$$

For $v \in R = \{v^*\} \bigcup L \backslash \{l\}$, and $b \in \{0,1\}$, the value of q^b_v is

$$q^b_v = \prod_{v''\in \text{children}(v)} q^b_{v''}. \tag{16}$$

For the cell nodes that are the leaves of the tree $q^b_v = q^b_{c,l}$.

2.7.1. Detection of SNVs for individual cells. Given a fixed CNA tree (denoted by t) and the read counts data (y^{SNV} denoted by y for simplicity), here the goal is to calculate the posterior distribution of $x^{SNV}_{c,l}$, the mutation status of locus l at cell c, which we denote by $x_{c,l}$ for simplicity.

The joint probability distribution of $x_{c,l}$, y and t can be written as:

$$p(x_{c,l}, y, t) = \sum_{v\in R}\sum_{t'\in\mathcal{N}^l_v(t\backslash l)} p(x_{c,l}, t', y) \tag{17}$$

$$= \sum_{v\in R}\sum_{t'\in\mathcal{N}^l_v(t\backslash l)} p(x_{c,l}|t')p(y|t')p(t'), \tag{18}$$

where R is the set of all loci nodes in the tree (including the root) excluding locus l. The joint probability distribution is calculated as

$$p(x_{c,l} = 1, y, t) = \sum_{v\in\mathcal{P}(c,t)}\sum_{t'\in\mathcal{N}^l_v(t\backslash l)} p(y|t')p(t'). \tag{19}$$

The set $\mathcal{P}(c, t)$ denotes all nodes on the shortest path from cell c to the root of the tree (including the root and excluding the cell c node). An example of the path on an imaginary tree is depicted in Fig. 12. The nodes coloured in green belong to $\mathcal{P}(c, t)$. Therefore, the posterior probability distribution of $x_{c,l} = 1$ yields

$$p(x_{c,l} = 1|y, t) = \frac{p(x_{c,l} = 1, y, t)}{p(y, t)} = \frac{\sum_{v \in \mathcal{P}(c,t)} \sum_{t' \in \mathcal{N}_v^l(t \setminus l)} p(y|t')p(t')}{p(y, t)}. \tag{20}$$

Rewriting Equation (20) assuming uniform probability distribution for $p(t')$ yields:

$$\begin{aligned}
p(x_{c,l} = 1|y, t) &\propto \sum_{v \in \mathcal{P}(c,t)} \sum_{t' \in \mathcal{N}_v^l(t \setminus l)} p(y|t'), \\
&= \sum_{v \in \mathcal{P}(c,t)} \sum_{t' \in \mathcal{N}_v^l(t \setminus l)} \prod_{l' \in L} \prod_{c' \in C} p(y_{c',l'}|t'), \\
&= \sum_{v \in \mathcal{P}(c,t)} \sum_{t' \in \mathcal{N}_v^l(t \setminus l)} \prod_{\substack{l' \in L \\ l' \neq l}} \prod_{c' \in C} p(y_{c',l'}|t') \prod_{m' \in C} p(y_{c',l}|t'), \\
&= K_1 \sum_{v \in \mathcal{P}(c,t)} \sum_{t' \in \mathcal{N}_v^l(t \setminus l)} \prod_{c' \in C} p(y_{c',l}|t'), \\
&= K_1 \sum_{v \in \mathcal{P}(c,t)} \sum_{t' \in \mathcal{N}_v^l(t \setminus l)} \prod_{c' \in C_{\setminus v}} p(y_{c',l}|t') \prod_{c' \in L_v} p(y_{c',l}|t'),
\end{aligned}$$

where N denotes the set of all trait nodes, C denotes the set of all cell nodes, C_v denotes the cells that are a descendant of node v, and $C_{\setminus v}$ denotes the cells that are a not descendant of node v. The product of the likelihood contributions for non-descendant nodes can be calculated by taking the product of q_c^0 for all cells, divided by the ones that are descendant of v:

$$\prod_{c' \in C_{\setminus v}} q_{c'}^0 = \frac{q_{v^*}^0}{q_v^0}.$$

Therefore:

$$p(x_{c,l} = 1|y, t) \propto K_1 \sum_{v \in \mathcal{P}(c,t)} \frac{q_{v^*}^0}{q_v^0} \sum_{t' \in \mathcal{N}_v^l(t \setminus l)} \prod_{c' \in C_v} p(y_{c',l}|t'). \tag{21}$$

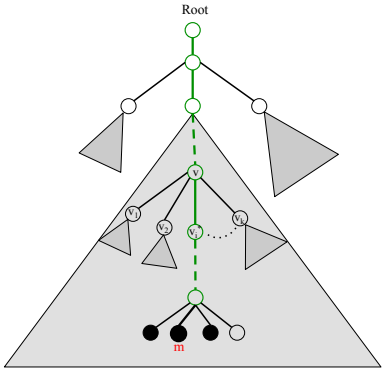

Figure 12 – A schematic view of the underlying tree inferred from CNA and SNV loci across multiple cells. Black and white nodes represent cells and loci, respectively. The grey triangle represents a subtree rooted at a node. It includes all of the nodes and edges in the subtree.

The likelihood contribution of descendant cells can be re-indexed by a binary vector $\mathbf{b} = (b_1, b_2, \ldots, b_k)$, where $b_i \in \{0, 1\}$, and $b_i = 1$ if the child v is to be moved into a child of the

node l. The value of k denotes the number of children of v. The i^*th child of v which is on the path from node v to cell c is called v_i^*. This implies $b_{i^*} = 1$ (See Fig. 12). Therefore:

$$\sum_{t' \in \mathcal{N}_v^l(t \setminus l)} \prod_{c' \in C_v} p(y_{c',l}|t') = q^1_{v_c^*} \sum_{b_1=0}^{1} \sum_{b_2=0}^{1} \dots \sum_{b_{i-1}=0}^{1} \sum_{b_{i+1}=0}^{1} \dots \sum_{b_k=0}^{1} \prod_{\substack{i=1 \\ i \neq i^*}}^{k} q^{b_i}_{v_i}. \tag{22}$$

Rewriting Equation (21) using Equation (22) yields:

$$\begin{aligned} p(x_{c,l} = 1|y, t) &\propto K_1 \sum_{v \in \mathcal{P}(c,t)} \frac{q^0_{v^*}}{q^0_v} q^1_{v_c^*} \sum_{b_1=0}^{1} \sum_{b_2=0}^{1} \dots \sum_{b_{i-1}=0}^{1} \sum_{b_{i+1}=0}^{1} \dots \sum_{b_k=0}^{1} \prod_{\substack{i=1 \\ i \neq i^*}}^{k} q^{b_i}_{v_i}, \\ &= K_1 \sum_{v \in \mathcal{P}(c,t)} \frac{q^0_{v^*}}{q^0_v} q^1_{v_c^*} \prod_{\substack{i=1 \\ i \neq i^*}}^{k} (q^0_{v_i} + q^1_{v_i}), \\ &= K_1 \sum_{v \in \mathcal{P}(c,t)} \frac{q^0_{v^*}}{q^0_v} \frac{\prod_{i=1}^{k} (q^0_{v_i} + q^1_{v_i})}{(q^0_{v_{i^*}} + q^1_{v_{i^*}})} q^1_{v_{i^*}}, \\ &= K_1 q^0_{v^*} \sum_{v \in \mathcal{P}(c,t)} \frac{q^1_{v_{i^*}}}{q^0_v (q^0_{v_{i^*}} + q^1_{v_{i^*}})} \prod_{i=1}^{k} (q^0_{v_i} + q^1_{v_i}). \end{aligned} \tag{23}$$

2.8. Computational complexity of the SNV calling algorithm

The computational complexity of Equation (23) is $O(|C| \cdot |L|)$ with $|C|$ the number of cells and $|L|$ the number of loci. In order to reduce the complexity of calculating $p(x_{c,l} = 1|y, t)$ for each locus and cell, $\mathcal{P}'(c, t)$ is defined to denote the nodes sitting on the path from root to cell c, excluding the root node and including the cell c node. Then,

$$q^*_v = \prod_{i=1}^{k} (q^0_{v_i} + q^1_{v_i}). \tag{24}$$

Therefore,

$$K_1 q^0_{v^*} \sum_{v \in \mathcal{P}(c,t)} \frac{q^1_{v_{i^*}}}{q^0_v (q^0_{v_{i^*}} + q^1_{v_{i^*}})} \prod_{i=1}^{k} (q^0_{v_i} + q^1_{v_i}) = K_1 q^0_{v^*} \sum_{v \in \mathcal{P}'(c,t)} \frac{q^1_v}{(q^0_v + q^1_v)} \frac{q^*_{\text{parent}(v)}}{q^0_{\text{parent}(v)}}.$$

Calculating $p(x_{c,l} = 1|y, t)$ with a recursive approach reduces the complexity from $O(|C||L|)$ to $O(|C| + |L|)$, where as in the last section L is the union of SNV and CNA loci.

3. Results

3.1. Sitka: scalable single cell phylogenetic tree inference

Fig. 1 shows the workflow of the sitka method. Sitka is based on a transformation of single cell copy number matrices retaining only presence or absence of changes in copy number profiles between contiguous genomic bins. This transformation allows us to approximate a complex evolutionary process (integer-valued copy numbers, prone to a high degree of homoplasy and dense dependence structure across sites) using a probabilistic version of a perfect phylogeny (see Fig. 2). We leverage the special structure created by the change point transformation to build a special purpose MCMC kernel, which has better computational scalability per move compared to classical phylogenetic kernels (Methods section 2.4.3).

We visualise the input data to sitka in a colour-coded matrix exemplified in Fig. 2-**a**. Each row in the matrix corresponds to an individual cell that has been sequenced in a single-cell platform. Each column in the matrix is a locus that is represented by a bin (a contiguous set of genomic positions). We assume that the integer copy number of each bin has been estimated as a preprocessing step, e.g., using a hidden Markov model (Zahn et al., 2017). In Fig. 2-**a** the copy number state is encoded by the colour of each entry in the matrix.

The output of sitka includes two types of directed rooted trees. Type I is the tree used for MCMC sampling in the inference procedure, and type II, which is derived from type I, is used in visualisation (Fig. 11-**a-c**). The set of nodes in a type I tree is given by the union of the cells, the CN change points (markers) under study, and a root node v^*. The topology of a type I tree bears the following phylogenetic interpretation: given a cell c in the tree, c is hypothesized to harbour the markers in the shortest path between c and the root node v^*, and only those markers. We enforce the constraint that all cells are leaf nodes, while markers can be either internal or leaf nodes. Markers placed at the leaves are interpreted as outliers, for example measured CN change points that are false positives.

To convert a type I tree to a type II tree, we remove from the type I tree all marker nodes that are leaf nodes, i.e., markers that are not present in any cells. We also collapse into a single node, the list of connected marker nodes that have exactly one descendent (i.e., chains). Fig. 13 shows a small *type I tree*, its transformation to a *type II tree* and the respective marker matrix. We visualise the input matrix and the estimated tree simultaneously by sorting the individual cells (rows of the matrix) such that they line up with the position of the corresponding leaves of the tree.

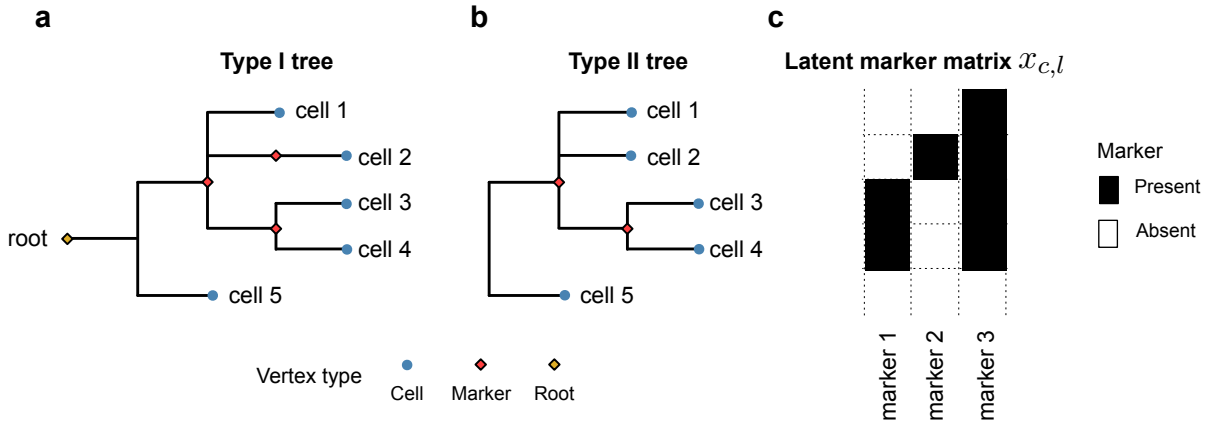

Figure 13 – A small type I tree t (**a**), its transformation into a type II tree (**b**), and the corresponding marker matrix $x = (x_{c,l})$ (**c**). The red nodes in (**a**) correspond from top to bottom to markers 2, 3, 1 in this order. Given a tree t, the latent marker matrix x is a deterministic function $x = x(t)$. Note that the clade comprising single-cells 3 and 4 has support in both markers 1 and 3. For clarity, we do not visualise type I trees, but plot their transformation, i.e., type II trees as follows. We remove from the type I tree all marker nodes that have $x_{c,l} = 0$ for all single-cells c. Lists of connected edges that have exactly one descendent (i.e., chains) are also collapsed into a single edge, e.g., the edge corresponding to markers 2 and 3 are collapsed into one edge (since marker 2 has only one descendent, namely single-cell 2).

Sitka uses change points as phylogenetic traits modelled using a relaxation of the perfect phylogeny assumption. For a phylogenetic tree, the perfect phylogeny assumption holds if and only if for all markers l, l changes at most once from its ancestral state over the tree. Change points arising from non-overlapping CNA events (i.e., such that the genomic locations affected by the CN event do not intersect) preserve the perfect phylogeny assumption. Fig. 14 shows examples of overlapping CNA events and their effect on markers. The two scenarios that can lead to the violation of the perfect phylogeny assumption are (i) when a CNA gain event is followed by an overlapping loss event or (ii) when a loss event is followed by an overlapping loss event, and the second event removes either end-point of the first event. For both (i) and (ii), a violation occurs only when the second overlapping event hits the same copy as the first event.

Imposing a perfect phylogeny on the *observed* change points is restrictive, as we expect both violations of the assumptions (e.g., due to homoplasy), and measurement noise. To address this we use an observation model (Methods section 2.4.1) which assigns positive probability to arbitrary deviations from the perfect phylogeny assumption, while encouraging configurations

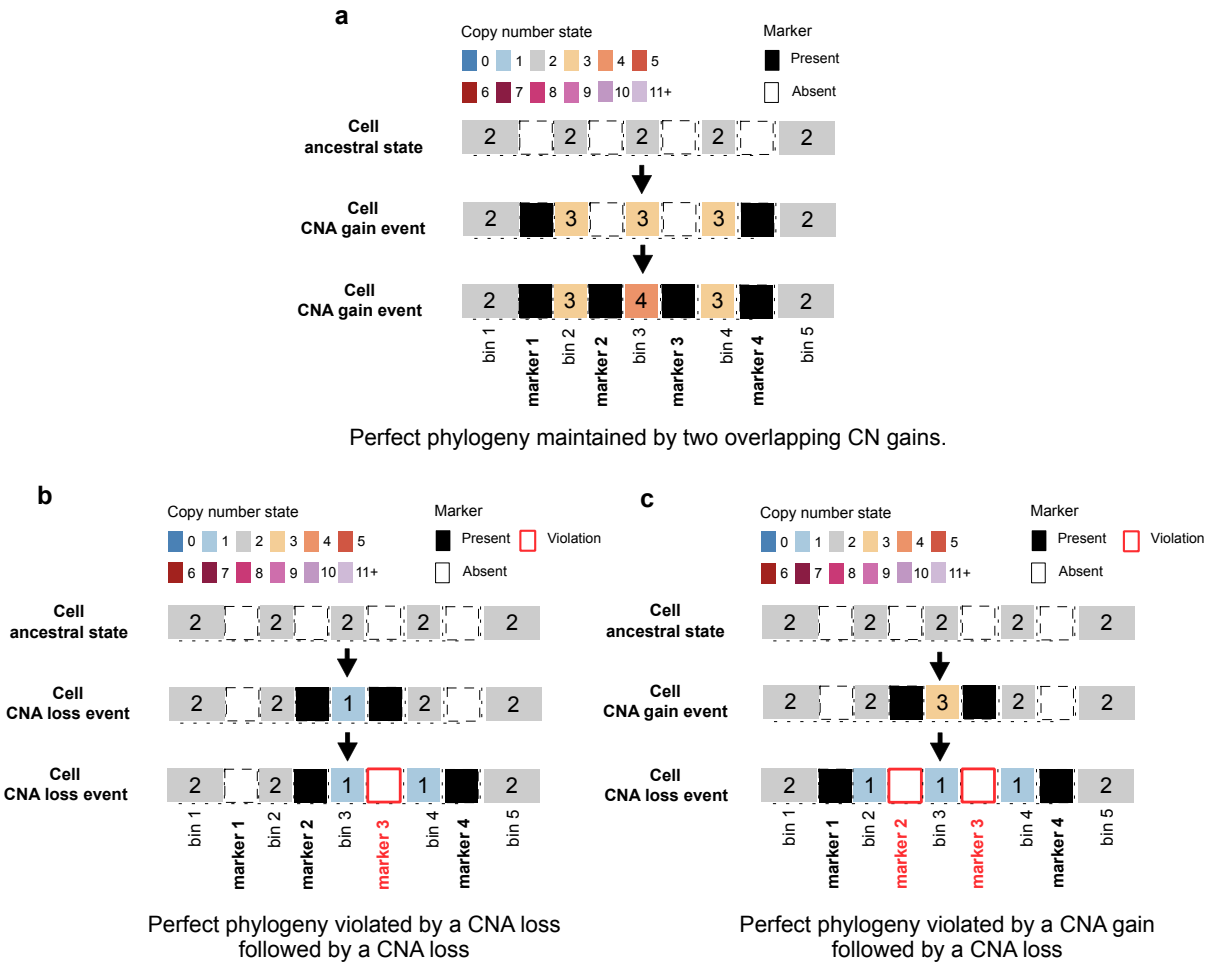

Figure 14 – The effects of overlapping CNA events on the perfect phylogeny assumption. A segment of a chromosome with five consecutive bins and their four corresponding markers are shown. Each panel follows the CN states interlaced with markers for a cell at the ancestral state (top), after a CNA event (middle), and after a second overlapping CNA event (bottom). The numbers in the CNA squares show the integer CN state (e.g., the ancestral state has two copies of the 5-bins long segment). (**a**) Two overlapping CNA gains maintain the perfect phylogeny assumption. If the infinite site assumption holds, it is unlikely for the end-points of the two gain events to exactly match. The same argument holds for a CNA loss followed by a CNA gain event. Note that in these cases, once a change point is acquired, it is not lost. (**b**) If a loss event is followed by another loss event in which either end-points of the first event is removed, the perfect phylogeny assumption will be violated (e.g., marker 3 is lost after the second loss event). Note that a violation does not occur if the loss events hit different copies of a segment. (**c**) Similarly, if a gain event is followed by a loss event, only if the latter erases the end-points of the former is the perfect phylogeny violated. Note how marker 2 and marker 3 are lost after the second CNA event.

where few markers and cells are involved in violations. Subsequently we impose the perfect phylogeny assumption on a *latent* maker matrix defined as follows. Given a type I tree t, the latent marker matrix x is a deterministic function $x = x(t)$. We compute $x : t \to \{0,1\}^{C \times L}$ by setting $x_{c,l} = 1$ if the single-cell c is a descendent of the marker node l in tree t, and otherwise $x_{c,l} = 0$. We use $y_{c,l}$ to refer to the observed change point l in individual cell c (Methods section 2.4.1).

Synthetic experiments show that sitka's performance decreases roughly linearly as a function of the rate of the key types of expected violation of the perfect phylogeny assumption (Fig. 8-**a,b**, Methods section 2.5).

3.2. Performance of sitka relative to alternative approaches

We compare the performance of sitka to alternative approaches (Section 2 of the supplementary text) on three scWGS datasets introduced here (Fig. 11-**a-c**). The first dataset, *SA*535, is generated for this project and contains 679 cells from three passages of a triple negative breast cancer (TNBC) patient derived xenograft sample. Passages X1, X5, and X8 had 62, 369, and 231 cells post quality filtering (Methods section 2.1) respectively. We also include 17 mostly diploid control cells. These cells are combined to generate the input to the analysis pipeline (Fig. 15).

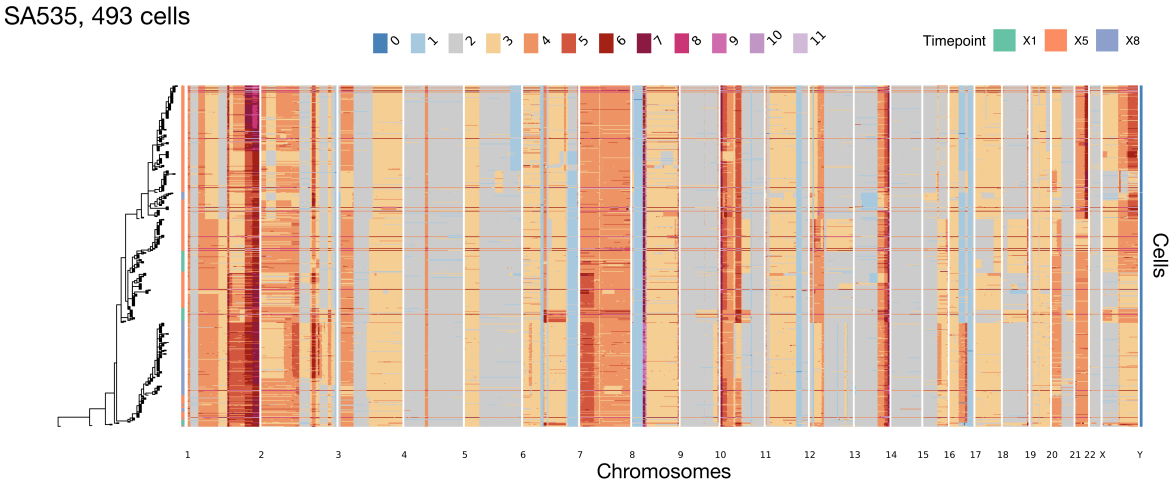

Figure 15 – Phylogenetic tree and CNA profile heatmap for the SA535 dataset. The rows of the heatmap are sorted according to the placement of cells on the phylogenetic tree. The columns of the heatmap are sorted by their genomic position.

The second dataset, labelled *OVA* (Laks et al., 2019), consists of cells from three samples taken from a patient with high grade serous (HGS) ovarian cancer. The first sample, *SA*1090, was from an ascites pre-treatment, while *SA*922 was from an ascites post-treatment. The third sample, *SA*921, was taken from the ovary. See Fig. 16 for the tree and the CNA profile heatmap for this dataset.

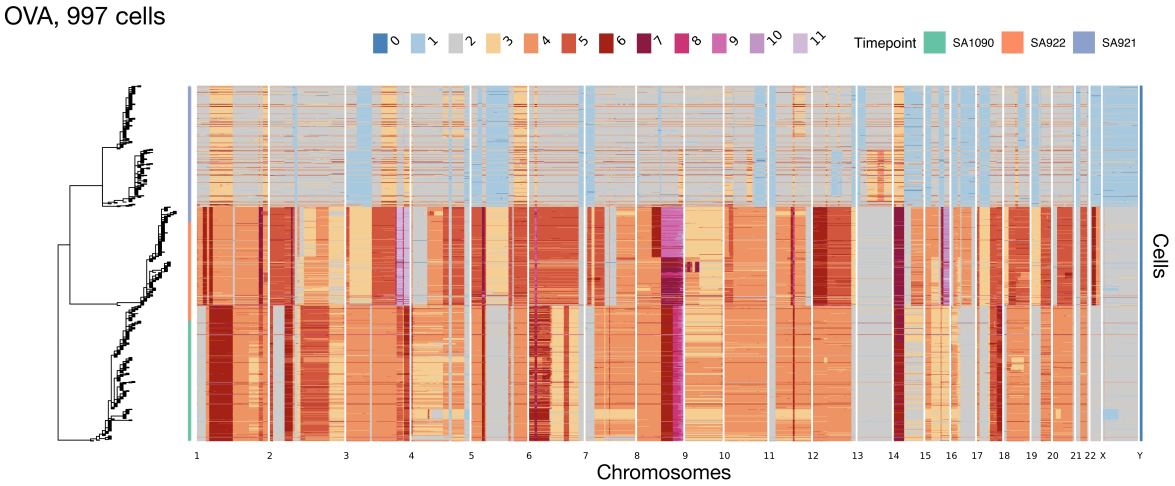

Figure 16 – Phylogenetic tree and CNA profile heatmap for the *OVA* dataset. The nearly diploid cells with the loss of heterozygosity on chromosome X are from SA1090. The cells with an amplification on chromosome 22 are from SA922. The rest belong to SA921.

The final dataset, *SA*501 (Laks et al., 2019), is another TNBC xenograft tumour from 6 untreated passages, namely X2, X5, X6, X8, X11, and X15. After filtering, 515, 236, 328, 189, 836,

and 308 cells remain in each passage respectively (for a total of 2,412 cells, see Fig. 17). Supplementary Table 2 shows the attrition after each step of filtering cells per passage in each dataset.

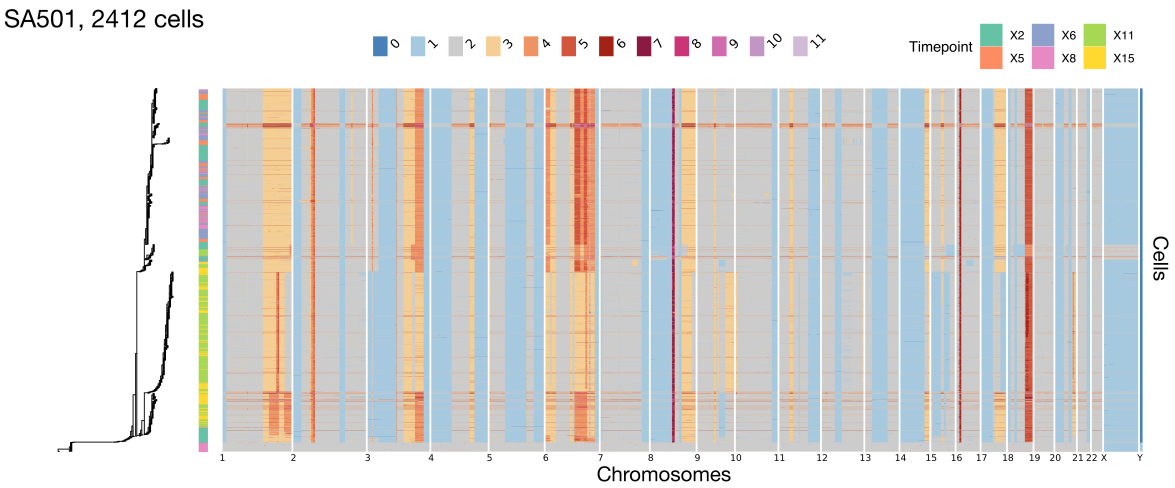

Figure 17 – Phylogenetic tree and CNA profile heatmap for the SA501 dataset. Note that the diploid cells at the bottom of the heatmap are control cells that were included in the experiment.

To evaluate inferred trees from sitka and other tree reconstruction methods, we use a goodness of fit performance metric, which compares the compatibility of observed CN change points with a given phylogeny using Youden's J index (Methods section 2.6, Fig. 11-**d**). Sitka has the highest Youden's index across all three datasets. `UPGMA` and `WPGMA` perform similarly on *SA*501 and *SA*535. `UPGMA` performs slightly better than `WPGMA` on the *OVA* dataset. `HDBSCAN` has a close but slightly smaller Youden's index than `UPGMA` over the *SA*535 and *OVA* datasets, but performs marginally better on *SA*501. `NJ` trails `WPGMA` on *SA*501 and the *OVA* datasets, and has the lowest Youden's index on *SA*535. `MrBayes` performs well on the smallest dataset, *SA*535, with `MrBayes-np2` and `MrBayes-np8` performing similar to `WPGMA`, and `MrBayesWithBinaryInput` having achieved the second highest Youden's index. On the *OVA* data, `MrBayesWithBinaryInput` and `MrBayes-np2` trail behind `medicc2` and `MEDALT`, while `MEDALTWithBinaryInput` has the lowest Youden's index among all methods on all datasets. `MrBayesWithBinaryInput` and `MrBayes-np2` trail behind `NJ` over the *SA*501 dataset. `medicc2` and `MEDALT` without binary input, ran with default settings, did not yield a result given our available computational budget, with the former not finishing after several days, and the latter running out of memory (144 GB). Following Eirew et al., 2015, we run `MrBayes` for 10,000,000 generations. `MrBayes-np8` had completed only 278,000 iterations running on *SA*501 after several days. The results in this comparison suggest that sitka performs better than the baseline methods. While due to limitation to our available computational budget, we could not allocate more time to the benchmarked methods, it is possible that given more runtime/computation budget, the other methods might have converged to more accurate solutions. Running sitka on the real-world datasets took on average 22.3, 46.6, and 12.9 hours for the *OVA*, *SA*501, and *SA*535 datasets respectively, on a Linux workstation with 72 Intel Xeon Platinum 8272CL 2.60GHz CPU processors and 144 GB of memory.

3.3. Single cell resolution phylogenetic inference in PDX

Here we analyse the foregoing three multi-sample datasets. To visualise the tree inference results we arrange the inferred consensus tree t (Methods section 2.4.5) and the cell-by-bin CN matrix side by side where the rows of the matrix correspond to the position of individual cells on the tree and the markers are arranged by their genomic position (Fig. 1-**h**). Fig. 11-**a-c** shows examples of the multi-channel visualisation where each marker is represented by a tuple of three different data-types or *channels*, namely: (i) the latent markers induced by the consensus

tree, $x(t)$; (ii) the matrix of marginal posterior probability that cell c is a descendent of marker l, computed via the average $\bar{m}$ (Fig. 1-**g**, Methods section 2.4.5); and (iii) the sitka transformed input data $y_{c,l}$.

We use this view to assess potential discrepancies between the input data and the inferred tree. In most cells and markers (as quantified in Fig. 18), the observed data is in close agreement with the inferred tree. In the following we provide some examples of disagreements. Consider first the ChrX in the *OV2295* dataset (Fig. 11-**a**). ChrX has a long orange band (inferred marker in channel (i)) not matched by a black band (observed marker in channel (iii)) suggesting that a perfect phylogeny violation has occurred.

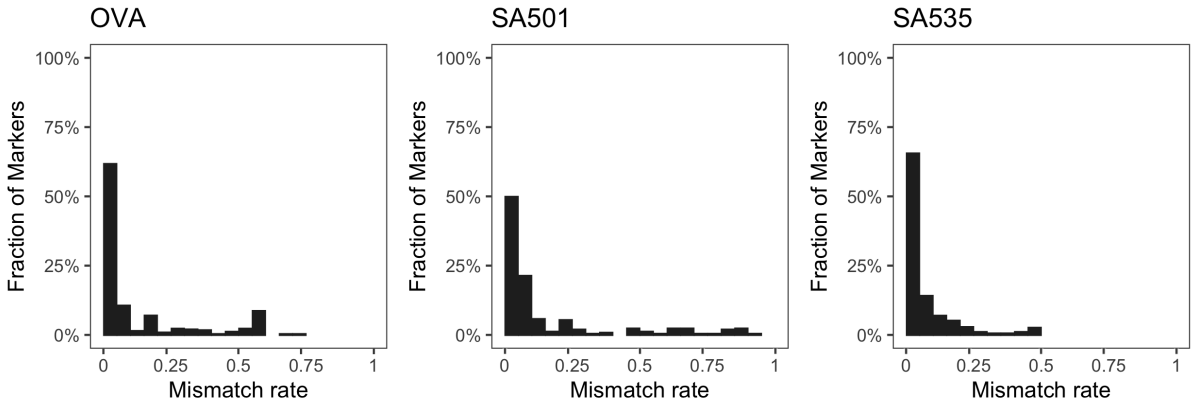

Figure 18 – The distribution of mismatch rate defined as the fraction of cells that have a mismatch between the inferred and jitter-fixed value of a marker.

The pattern in this marker is consistent with the presence of an ancestral event followed by a deletion. In Fig. 11-**b**, a set of diploid cells are attached to the root of the tree. These are control cells included in the experiment and correspond to a region in the bottom of the matrix with no inferred markers (orange bands) and almost no observed markers (black bands). In this dataset, there are change points where the observed marker has a high density (black band), but the tree is reconstructed with the marker absent (no matching orange band). Examples can be found in Chr1, Chr7 and Chr16. One possible explanation could be that the end-points of each event were detected as slightly shifted across cells. For instance, in Fig. 17 there are two bins with an amplification (CN state equal to three) in Chr1p where cells that harbour a mutation in the first bin appear not to have a mutation in the second bin, suggesting that the same event was called in the first bin in some cells, and in the second bin in others. An alternative hypothesis is that the cells in this dataset have a mutator phenotype that promotes CN mutations in these bins.

Fig. 18 shows the distribution of mismatch rates for each dataset, defined as the fraction of times that the observed and inferred markers do not match, i.e., $\frac{1}{C}\sum_{c\in C}\mathbf{1}[y_{c,l} \neq x_{c,l}]$ for $l \in L$ (corresponding to the black and orange bands in Fig. 11-**a**). In *OV2295*, 41 markers (11%) have a mismatch rate of over 50%, where marker *chr15_67000001_67500000* has the highest mismatch rate at 70%. In SA501, 30 markers (11%) have a mismatch rate of over 50%, 13 of which (5%) have a mismatch rate of over 75%. SA535 has the lowest maximum mismatch rate at 49% (marker *15_72000001_72500000*). See Section 3 of the supplementary text for a discussion of the tree shape statistics for these datasets.

3.4. Placement of SNVs using the CNA inferred tree

To determine the presence or absence of SNVs in cells using data with high levels of missingness, we develop an extension of sitka, the sitka-snvmodel. Given single cell level variant read counts, the model incorporates CN data to place SNVs on the sitka-inferred phylogenetic tree. This *backbone* CN tree provides a principled way to pool statistical strength across groups of single cells sequenced at low coverage, including data from the DLP+ platform (Zahn et al., 2017). The output of the sitka-snvmodel is an *extended* tree that has marker nodes that comprise SNVs in addition to the original CNAs.

The SNVs are added to the existing CNA-based tree with the computational complexity of $O(|C|+|L|)$ per SNV. Fig. 8-**c** shows the result of SNV placement with the number of variant reads in *SA*535, corresponding to the tree shown in Fig. 11-**c**. Figs. 19, 20, and 21 show the number of variant reads and the matching SNV call probabilities for the *SA*535, *OVA* and *SA*501 datasets respectively. Sitka and sitka-snvprovide a comprehensive genomic analysis tool for large scale low-coverage scWGS.

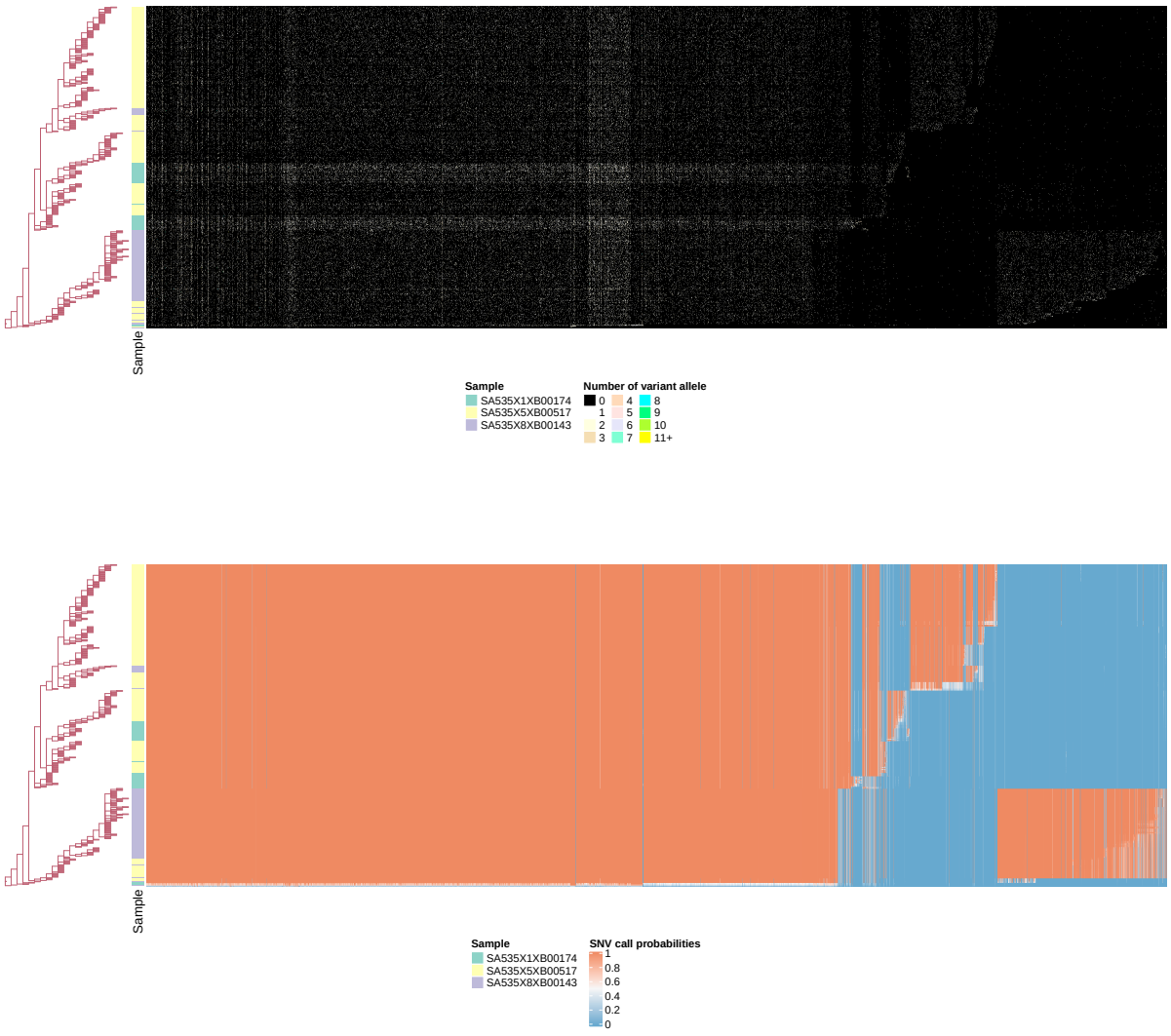

Figure 19 – SNV variant reads data and SNV call probabilities for SA535 dataset beside the underlying phylogenetic tree.

4. Discussion

Our method ignores certain pairwise dependencies induced by copy number change events having two end-points (except in cases where one of the end points is the end of the chromosome, e.g., whole-chromosome-arm events). This artificial duplication of the events having two input end-points can lead to the method being overconfident, i.e., outputting credible intervals that are smaller than expected. This is partly a reason for focusing more on point estimates (consensus trees) in this work, which we expect are less affected by this phenomenon (see Section 2.5.2).

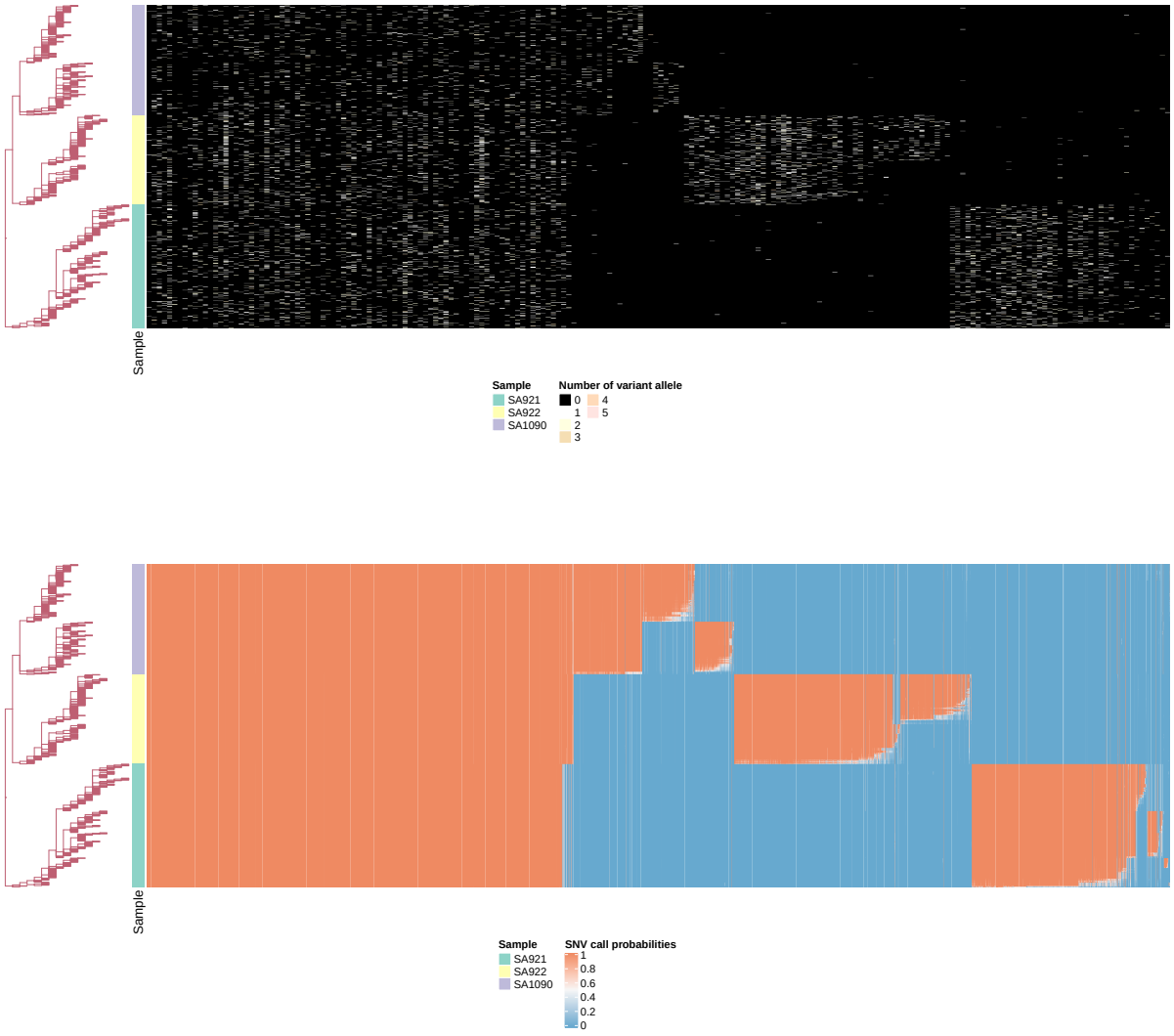

Figure 20 – SNV variant reads data and SNV call probabilities for OVA dataset beside the underlying phylogenetic tree..

In the present study we use data in which the genome of the single cells CNA profiles are partitioned into bins of a fixed size (500Kb), each assigned a constant integer CN state. The relatively large size is due to the low coverage inherent to the scWGS platform, but it implies that the same bin may harbour multiple CNA events. Biological processes that result in complex DNA rearrangements could further increase the probability of having two hits in one bin (Mishra and Whetstine, 2016; Yi and Ju, 2018). Post hoc inspection is necessary to rule out large violations of our assumptions. This highlights the importance of our goodness-of-fit and visualisation methods as they help detecting such violations.

We note that we lose information when applying the sitka transformation. This transformation is necessary for the computational feasibility of the likelihood. In absence of this relaxation, the computational complexity of each iteration of the MCMC algorithm may no longer be bounded by $O(|C|+|L|)$. Indeed, the approach to efficiently compute the likelihood depends on binary latent variables with specific perfect phylogeny assumptions, and it is not clear how to generalize this calculation to models that keep track of the evolution of more detailed CN state information along the phylogeny.

Structural variations such as chromothripsis, that affect multiple segments of the genome at the same time, make it difficult to determine the rate of CNA events and suggest that CNA

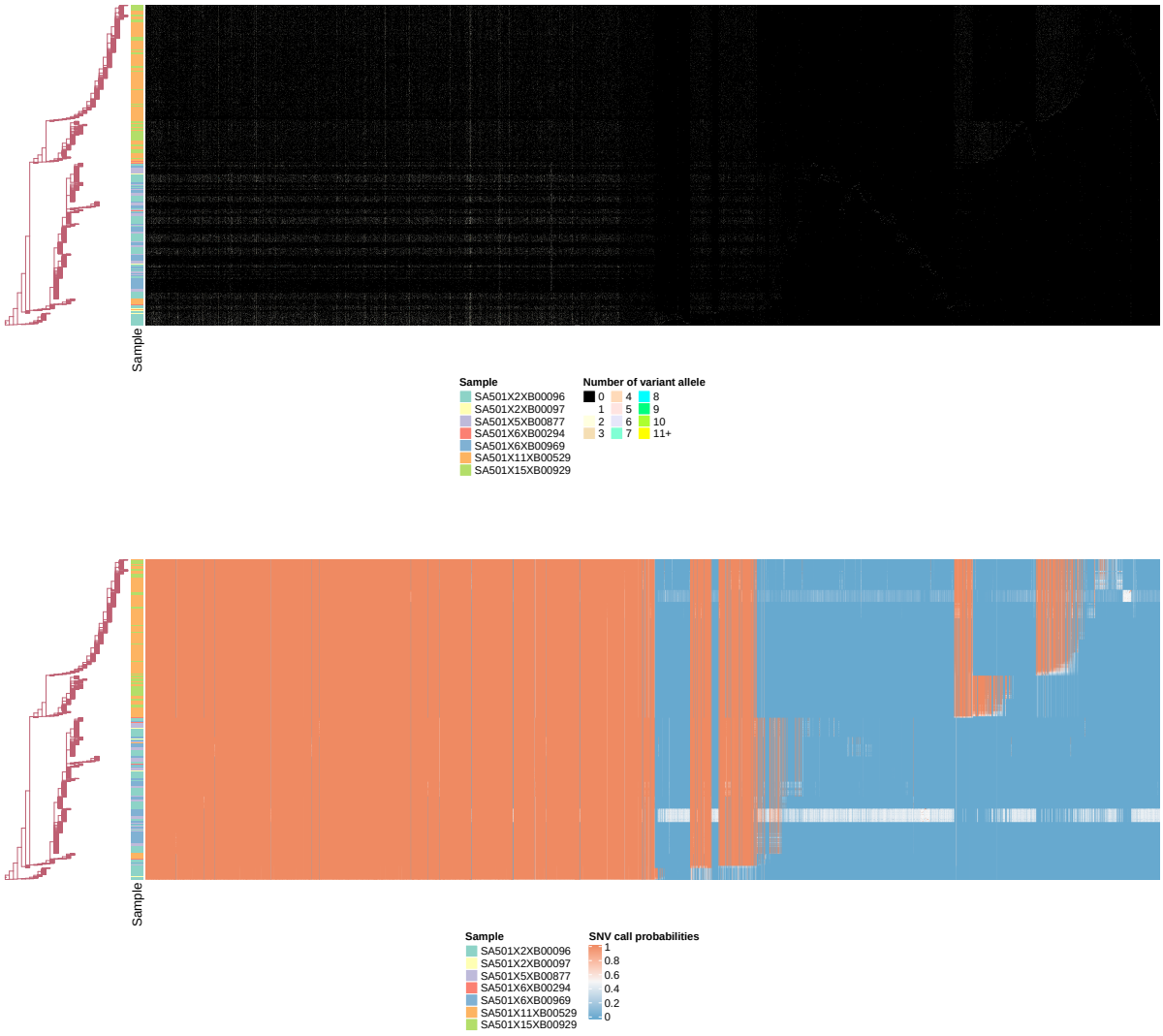

Figure 21 – SNV variant reads data and SNV call probabilities for SA501 dataset beside the underlying phylogenetic tree.

events may not be suitable molecular clocks to estimate branch lengths. One possible remedy is to first infer the tree topology via markers based on CNA events and then conditioned on this topology, add SNVs to the tree. The number of SNVs on each edge of the tree may be used to inform branch lengths.

Our preprocessing pipeline excludes multiple cells from the analysis (see Supplementary Table 2). We filter out a fraction of cells to remove contaminated cells, either doublets (DNA material from two cells that is inadvertently merged) or mouse cells (in our real world datasets, we study human tumours that were transplanted into mice), cells with too many erroneous sequencing artefacts, and cycling cells (in the process of replicating their DNA). Removing a portion of the sequenced cells will decrease the statistical power to determine the subclonal structure of the population—an important application of this work—, and may bias the sampling against clones that have a higher division rate. We expect this will be an intrinsic limitation to any scWGS phylogenetic methods and this motivates the design of improved classification methods detecting cell cycling from genomic and imaging data.

We developed two main variants of our Bayesian models, one with error rate parameters shared by all loci (global) and one with locus-specific (local) error rates. In our simulation experiments, the global and local parameterizations performed similarly. Based on the similar performance of these two models and the fact that the global parameterization is computationally cheaper, we recommend the use of the global parameterization by default.

Evaluating the performance of a phylogenetic reconstruction method on real-world datasets is difficult, mainly due to a paucity of ground truth. One promising area of research is the use of CRISPR-Cas9 based lineage tracing (Quinn et al., 2021). In absence of ground truth data, we developed a goodness-of-fit framework that to our knowledge enables a first of a kind benchmarking of phylogenetic inference methods over real-world scWGS CNA datasets.

Phylogenetic tree reconstruction is a principled way to identify subpopulations in a heterogeneous single-cell population. This in turn enables the use of population genetics models that track the abundance of subpopulations over multiple timepoints (Salehi et al., 2021) and to make inferences about the evolutionary forces acting on each clone. Further study with timeseries modelling will provide insight into therapeutic strategies promoting early intervention, drug combinations and evolution-aware approaches to clinical management.

Acknowledgements

Preprint version 5 of this article has been peer-reviewed and recommended by Peer Community In Mathematical and Computational Biology (https://doi.org/10.24072/pci.mcb.100112) Lambert, 2023. We extend our gratitude to Sarah P. Otto for her helpful comments on a draft of this manuscript.

Fundings

This project was generously supported by the BC Cancer Foundation at BC Cancer and Cycle for Survival supporting Memorial Sloan Kettering Cancer Center. SPS holds the Nicholls Biondi Chair in Computational Oncology and is a Susan G. Komen Scholar (#GC233085). SA holds the Nan and Lorraine Robertson Chair in Breast Cancer and is a Canada Research Chair in Molecular Oncology (950-230610). Additional funding provided by the Terry Fox Research Institute Grant 1082, Canadian Cancer Society Research Institute Impact program Grant 705617, CIHR Grant FDN-148429, Breast Cancer Research Foundation award (BCRF-18-180, BCRF-19-180 and BCRF-20-180), MSK Cancer Center Support Grant/Core Grant (P30 CA008748), National Institutes of Health Grant (1RM1 HG011014-01), CCSRI Grant (#705636), the Cancer Research UK Grand Challenge Program, Canada Foundation for Innovation (40044) to SA, SPS and ABC.

Conflict of interest disclosure

The authors declare that they comply with the PCI rule of having no financial conflicts of interest in relation to the content of the article. S.P.S. and S.A. are founders, shareholders, and consultants of Imagia Canexia Health Inc.

Data, script, code, and supplementary information availability

Data are available online: https://doi.org/10.5281/zenodo.8051016 (Salehi, 2023), https://doi.org/10.1016/j.cell.2019.10.026 (Laks et al., 2019) (Laks et al. 2019), and https://doi.org/10.5281/zenodo.3445364 (McPherson, 2019); script and codes are available online: https://doi.org/10.5281/zenodo.8050973 (Salehi et al., 2023); supplementary information is available online: https://doi.org/10.5281/zenodo.8078323; Sitka is available at https://github.com/UBC-Stat-ML/sitkatree.git.

5. Author Contributions

SS, FD: computational method development, data analysis, manuscript writing; KC: data analysis, manuscript writing; KRC, AR: method development; FK, data generation; DL, MA, AM, MW, TF: computational biology, data analysis; NR: manuscript editing; SA: data generation and oversight; SPS: method development and oversight; ABC: project conception and oversight, statistical inference method development, manuscript writing, senior responsible author.

6. References

Abbosh C, Birkbak NJ, Wilson GA, Jamal-Hanjani M, Constantin T, Salari R, Le Quesne J, Moore DA, Veeriah S, Rosenthal R, et al. (2017). *Phylogenetic ctDNA analysis depicts early-stage lung cancer evolution*. *Nature* **545**, 446–451. https://doi.org/10.1038/nature22364.

Aldous D (1996). *Probability distributions on cladograms*. In: *Random discrete structures*. Springer, pp. 1–18. https://doi.org/10.1007/978-1-4612-0719-1_1.

Baslan T, Kendall J, Rodgers L, Cox H, Riggs M, Stepansky A, Troge J, Ravi K, Esposito D, Lakshmi B, et al. (2012). *Genome-wide copy number analysis of single cells*. *Nature protocols* **7**, 1024–1041. https://doi.org/10.1038/nprot.2012.039.

Blum MGB, François O (2006). *Which random processes describe the tree of life? A large-scale study of phylogenetic tree imbalance*. *Systematic Biology* **55**, 685–691. https://doi.org/10.1080/10635150600889625.

Bortolussi N, Durand E, Blum M, François O (2006). *apTreeshape: statistical analysis of phylogenetic tree shape*. *Bioinformatics* **22**, 363–364. https://doi.org/10.1093/bioinformatics/bti798.

Bouchard-Côté A, Chern K, Cubranic D, Hosseini S, Hume J, Lepur M, Ouyang Z, Sgarbi G (2022). *Blang: Probabilitistic Programming for Combinatorial Spaces*. *Journal of Statistical Software* **103**, 1–98. https://doi.org/10.18637/jss.v103.i11.

Campello RJ, Moulavi D, Sander J (2013). *Density-based clustering based on hierarchical density estimates*. In: *Pacific-Asia conference on knowledge discovery and data mining*. Springer, pp. 160–172. https://doi.org/10.1007/978-3-642-37456-2_14.

Coronado TM, Mir A, Rosselló F, Rotger L (2020). *On Sackin's original proposal: the variance of the leaves' depths as a phylogenetic balance index*. *BMC bioinformatics* **21**, 1–17. https://doi.org/10.1186/s12859-020-3405-1.

Desper R, Gascuel O (2002). *Fast and accurate phylogeny reconstruction algorithms based on the minimum-evolution principle*. In: *International Workshop on Algorithms in Bioinformatics*. Springer, pp. 357–374. https://doi.org/10.1089/106652702761034136.

Eirew P, Steif A, Khattra J, Ha G, Yap D, Farahani H, Gelmon K, Chia S, Mar C, Wan A, et al. (2015). *Dynamics of genomic clones in breast cancer patient xenografts at single-cell resolution*. *Nature* **518**, 422–426. https://doi.org/10.1038/nature13952.

Gao R, Davis A, McDonald TO, Sei E, Shi X, Wang Y, Tsai PC, Casasent A, Waters J, Zhang H, et al. (2016). *Punctuated copy number evolution and clonal stasis in triple-negative breast cancer*. *Nature genetics* **48**, 1119. https://doi.org/10.1038/ng.3641.

Gawad C, Koh W, Quake SR (2016). *Single-cell genome sequencing: current state of the science*. *Nature Reviews Genetics* **17**, 175. https://doi.org/10.1038/nrg.2015.16.

Geman S, Geman D (1984). *Stochastic relaxation, Gibbs distributions, and the Bayesian restoration of images*. *IEEE Transactions on pattern analysis and machine intelligence*, 721–741. https://doi.org/10.1109/TPAMI.1984.4767596.

Greenman CD, Pleasance ED, Newman S, Yang F, Fu B, Nik-Zainal S, Jones D, Lau KW, Carter N, Edwards PAW, Futreal PA, Stratton MR, Campbell PJ (2012). *Estimation of rearrangement phylogeny for cancer genomes*. *Genome Research* **22**, 346–361. https://doi.org/10.1101/gr.118414.110.

Guindon S, Gascuel O (2003). *A simple, fast, and accurate algorithm to estimate large phylogenies by maximum likelihood*. *Systematic Biology* **52**, 696–704. https://doi.org/10.1080/10635150390235520.

Househam J, Heide T, Cresswell GD, Spiteri I, Kimberley C, Zapata L, Lynn C, James C, Mossner M, Fernandez-Mateos J, et al. (2022). *Phenotypic plasticity and genetic control in colorectal cancer evolution*. *Nature*, 1–10. https://doi.org/10.1038/s41586-022-05311-x.

Huelsenbeck JP, Ronquist F (2001). *MRBAYES: Bayesian inference of phylogenetic trees*. *Bioinformatics* **17**, 754–755. https://doi.org/10.1093/bioinformatics/17.8.754.

Jahn K, Kuipers J, Beerenwinkel N (2016). *Tree inference for single-cell data*. *Genome Biology* **17**, 86. https://doi.org/10.1186/s13059-016-0936-x.

Kaufmann TL, Petkovic M, Watkins TB, Colliver EC, Laskina S, Thapa N, Minussi DC, Navin N, Swanton C, Van Loo P, et al. (2022). *MEDICC2: whole-genome doubling aware copy-number phylogenies for cancer evolution*. *Genome biology* **23**, 241. https://doi.org/10.1186/s13059-022-02794-9.

Kingman JFC (1982). *The coalescent*. *Stochastic processes and their applications* **13**, 235–248. https://doi.org/10.1016/0304-4149(82)90011-4.

Kuhner MK, Felsenstein J (1994). *A simulation comparison of phylogeny algorithms under equal and unequal evolutionary rates*. *Molecular Biology and Evolution* **11**, 459–468. https://doi.org/10.1093/oxfordjournals.molbev.a040126.

Laks E, McPherson A, Zahn H, Lai D, Steif A, Brimhall J, Biele J, Wang B, Masud T, Ting J, Grewal D, Nielsen C, Leung S, Bojilova V, Smith M, Golovko O, Poon S, Eirew P, Kabeer F, Ruiz de Algara T, et al. (2019). *Clonal Decomposition and DNA Replication States Defined by Scaled Single-Cell Genome Sequencing*. *Cell* **179**, 1207–1221.e22. https://doi.org/10.1016/j.cell.2019.10.026.

Lambert A (2023). *"Phylogenetic reconstruction from copy number aberration in large scale, low-depth genome-wide single-cell data*. https://doi.org/10.24072/pci.mcb.100112.

Leung ML, Davis A, Gao R, Casasent A, Wang Y, Sei E, Vilar E, Maru D, Kopetz S, Navin NE (2017). *Single-cell DNA sequencing reveals a late-dissemination model in metastatic colorectal cancer*. *Genome research* **27**, 1287–1299. https://doi.org/10.1101/gr.209973.116.

Ma J, Ratan A, Raney BJ, Suh BB, Miller W, Haussler D (2008). *The infinite sites model of genome evolution*. *Proceedings of the National Academy of Sciences* **105**, 14254–14261. https://doi.org/10.1073/pnas.0805217105.

Malikic S, Jahn K, Kuipers J, Sahinalp SC, Beerenwinkel N (2019). *Integrative inference of subclonal tumour evolution from single-cell and bulk sequencing data*. *Nature communications* **10**, 1–12. https://doi.org/10.1038/s41467-019-10737-5.

Mallory XF, Edrisi M, Navin N, Nakhleh L (2020). *Methods for copy number aberration detection from single-cell DNA-sequencing data*. *Genome biology* **21**, 1–22. https://doi.org/10.1186/s13059-020-02119-8.

McPherson A (2019). *Clonal decomposition and DNA replication states defined by scaled single cell genome sequencing (Version v2) [Data set]*. Zenodo. https://doi.org/10.5281/zenodo.3445364.

Miller CA, White BS, Dees ND, Griffith M, Welch JS, Griffith OL, Vij R, Tomasson MH, Graubert TA, Walter MJ, et al. (2014). *SciClone: inferring clonal architecture and tracking the spatial and temporal patterns of tumor evolution*. *PLoS Comput Biol* **10**, e1003665. https://doi.org/10.1371/journal.pcbi.1003665.

Mishra S, Whetstine JR (2016). *Different Facets of Copy Number Changes: Permanent, Transient, and Adaptive*. *Molecular and Cellular Biology* **36**, 1050–1063. https://doi.org/10.1128/MCB.00652-15.

Neal R (2003). *Slice sampling*. *The Annals of Statistics* **31**, 705–767. https://doi.org/10.1214/aos/1056562461.

Neher RA, Hallatschek O (2013). *Genealogies of rapidly adapting populations*. *Proceedings of the National Academy of Sciences* **110**, 437–442. https://doi.org/10.1073/pnas.1213113110.

Paradis E (2011). *Analysis of Phylogenetics and Evolution with R*. Springer Science & Business Media. https://doi.org/10.1007/978-1-4614-1743-9.

Pellegrino M, Sciambi A, Treusch S, Durruthy-Durruthy R, Gokhale K, Jacob J, Chen TX, Geis JA, Oldham W, Matthews J, et al. (2018). *High-throughput single-cell DNA sequencing of acute*

myeloid leukemia tumors with droplet microfluidics. *Genome research* **28**, 1345–1352. https://doi.org/10.1101/gr.232272.117.

Quinn JJ, Jones MG, Okimoto RA, Nanjo S, Chan MM, Yosef N, Bivona TG, Weissman JS (2021). *Single-cell lineages reveal the rates, routes, and drivers of metastasis in cancer xenografts*. *Science* **371**, eabc1944. https://doi.org/10.1126/science.abc1944.

Robert C (2007). *The Bayesian Choice - From Decision-Theoretic Foundations | Christian Robert | Springer*. https://doi.org/10.1007/0-387-71599-1.

Robinson DF, Foulds LR (1981). *Comparison of phylogenetic trees*. *Mathematical biosciences* **53**, 131–147. https://doi.org/10.1016/0025-5564(81)90043-2.

Ross EM, Markowetz F (2016). *OncoNEM: inferring tumor evolution from single-cell sequencing data*. *Genome Biology* **17**, 69. https://doi.org/10.1186/s13059-016-0929-9.

Sainudiin R, Véber A (2016). *A Beta-splitting model for evolutionary trees*. *Royal Society open science* **3**, 160016. https://doi.org/10.1098/rsos.160016.

Saitou N, Nei M (1987). *The neighbor-joining method: a new method for reconstructing phylogenetic trees*. *Molecular biology and evolution* **4**, 406–425. https://doi.org/10.1093/oxfordjournals.molbev.a040454.

Salehi S (2023). *UBC-Stat-ML/sitka_data: Sitka data publication (Dataset)*. Zenodo. https://doi.org/10.5281/zenodo.8051016.

Salehi S, Dorri F, Chern K, Bouchard-Côté A (2023). *UBC-Stat-ML/sitkatree: Sitka publication (Code)*. Zenodo. https://doi.org/10.5281/zenodo.8050973.

Salehi S, Kabeer F, Ceglia N, Andronescu M, Williams MJ, Campbell KR, Masud T, Wang B, Biele J, Brimhall J, Gee D, Lee H, Ting J, Zhang AW, Tran H, O'Flanagan C, Dorri F, Rusk N, Algara TR, Lee SR, et al. (2021). *Clonal fitness inferred from time-series modelling of single-cell cancer genomes*. *Nature* **595**, 585–590. https://doi.org/10.1038/s41586-021-03648-3.

Satas G, Zaccaria S, Mon G, Raphael BJ (2020). *Scarlet: Single-cell tumor phylogeny inference with copy-number constrained mutation losses*. *Cell Systems* **10**, 323–332. https://doi.org/10.1016/j.cels.2020.04.001.

Schliep K (2011). *phangorn: phylogenetic analysis in R*. *Bioinformatics* **27**, 592–593. https://doi.org/10.1093/bioinformatics/btq706.

Schwartz R, Schäffer AA (2017). *The evolution of tumour phylogenetics: principles and practice*. *Nature Reviews Genetics* **18**, 213–229. https://doi.org/10.1038/nrg.2016.170.

Singer J, Kuipers J, Jahn K, Beerenwinkel N (2018). *Single-cell mutation identification via phylogenetic inference*. *Nature communications* **9**, 1–8. https://doi.org/10.1101/290908.

Sokal RR (1958). *A statistical method for evaluating systematic relationships. Univ. Kansas, Sci. Bull.* **38**, 1409–1438.

Som A (2009). *ML or NJ-MCL? A comparison between two robust phylogenetic methods*. *Computational Biology and Chemistry* **33**, 373–378. https://doi.org/10.1016/j.compbiolchem.2009.07.007.

Staab PR, Metzler D (2016). *Coala: an R framework for coalescent simulation*. *Bioinformatics* **32**, 1903–1904. https://doi.org/10.1093/bioinformatics/btw098.

Teh YW et al. (2010). *Dirichlet Process. Encyclopedia of machine learning* **1063**, 280–287. https://doi.org/10.1007/978-0-387-30164-8_219.

Wang F, Wang Q, Mohanty V, Liang S, Dou J, Han J, Minussi DC, Gao R, Ding L, Navin N, et al. (2021). *MEDALT: single-cell copy number lineage tracing enabling gene discovery*. *Genome biology* **22**, 1–22. https://doi.org/10.1186/s13059-021-02291-5.

Wang Y, Waters J, Leung ML, Unruh A, Roh W, Shi X, Chen K, Scheet P, Vattathil S, Liang H, et al. (2014). *Clonal evolution in breast cancer revealed by single nucleus genome sequencing*. *Nature* **512**, 155–160. https://doi.org/10.1038/nature13600.

Williams TL, Moret BME (2003). *An investigation of phylogenetic likelihood methods*. In: *Third IEEE Symposium on Bioinformatics and Bioengineering, 2003. Proceedings.* Pp. 79–86. https://doi.org/10.1109/BIBE.2003.1188932.

Wilson D (1996). *Generating Random Spanning Trees More Quickly Than the Cover Time*. In: *Proceedings of the Twenty-eighth Annual ACM Symposium on Theory of Computing*. STOC '96. New York, NY, USA: ACM, pp. 296–303. https://doi.org/10.1145/237814.237880.

Xu X, Hou Y, Yin X, Bao L, Tang A, Song L, Li F, Tsang S, Wu K, Wu H, He W, Zeng L, Xing M, Wu R, Jiang H, Liu X, Cao D, Guo G, Hu X, Gui Y, et al. (2012). *Single-Cell Exome Sequencing Reveals Single-Nucleotide Mutation Characteristics of a Kidney Tumor*. *Cell* **148**, 886–895. https://doi.org/10.1016/j.cell.2012.02.025.

Yi K, Ju YS (2018). *Patterns and mechanisms of structural variations in human cancer*. *Experimental & Molecular Medicine* **50**, 98. https://doi.org/10.1038/s12276-018-0112-3.

Youden WJ (1950). *Index for rating diagnostic tests*. *Cancer* **3**, 32–35. 10.1002/1097-0142(1950)3:1%3C32::aid-cncr2820030106%3E3.0.co;2-3.

Yu C, Yu J, Yao X, Wu WK, Lu Y, Tang S, Li X, Bao L, Li X, Hou Y, et al. (2014). *Discovery of biclonal origin and a novel oncogene SLC12A5 in colon cancer by single-cell sequencing*. *Cell research* **24**, 701–712. https://doi.org/10.1038/cr.2014.43.

Zafar H, Tzen A, Navin N, Chen K, Nakhleh L (2017). *SiFit: inferring tumor trees from single-cell sequencing data under finite-sites models*. *Genome biology* **18**, 1–20. https://doi.org/10.1186/s13059-017-1311-2.

Zahn H, Steif A, Laks E, Eirew P, VanInsberghe M, Shah S, Aparicio S, Hansen C (2017). *Scalable whole-genome single-cell library preparation without preamplification*. *Nature Methods* **14**, 167–173. https://doi.org/10.1038/nmeth.4140.

Supplementary Text: Cancer phylogenetic tree inference at scale from 1000s of single cell genomes

1. Pre-processing

In this section we give an overview of the preprocessing steps for inferring Sitka trees. These steps are summarised in Supplementary Fig. 1.

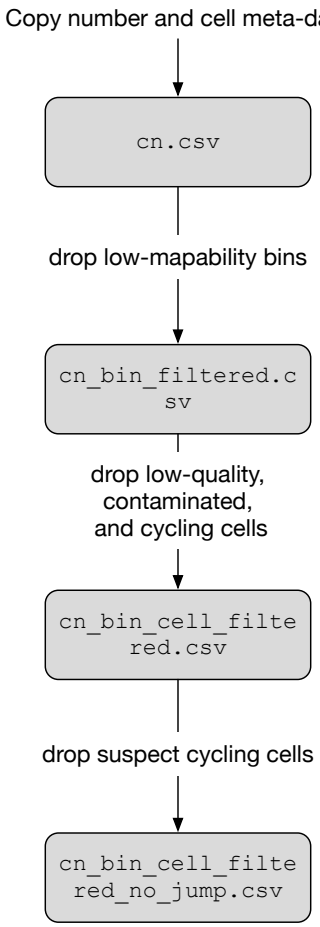

Supplementary Figure 1 – Filtering the CNA data for tree inference.

1.1. HMMcopy pre-processing

Corrected CNA states from `HMMCopy` are stored in `cn.csv.gz` and this file is the input to our preprocessing pipeline. For this work the data was stored in the cloud (Microsoft Azure) and the `scgenome` API was used to access and download the data. Please see https://github.com/shahcompbio/scgenome for documentation. The `scgenome` API ensures that only cells with the correct `sample_ids` are selected, removes control cells and cells that have fewer than 10,000 mapped reads.

1.2. Filtering low-mappability bins

Some copy number bins are located at parts of the genome where sequencing is difficult, for example due to inaccessibility of the genome at that position. This is reflected in their mappability score. We filter the CNA matrix to keep high-map-ability bins `cn_bin_filtered.csv.gz`. In this work we use a cutoff threshold of `map >=.99` that yields 4375/6206 or 0.705% of the bins. The list of kept bins is identical across all datasets.

1.3. Filtering low-quality cells

In this step, a second round of quality control is done. Cells with a *quality score*, as defined in Laks et al., 2019, of over 0.75 or higher are kept, while the other ones which are suspected to be contaminated (e.g., mouse cells) or cycling cells are removed. This results in `cn_bin_cell_filtered.csv.gz`.

1.4. Filtering cells with excess CNA changes

Some cells show a "jumpy" CNA profile in which there are too many copy number changes. It appears that these cells are either in early or late stages of division and were missed by the S-phase classifier. The CNA profile of early replicating cells is patterned by seemingly scattered focal amplifications while the late replicating cells show scattered focal deletions. Note that not all parts of the genome duplicate at the same time upon cell division. Regions that start duplicating later will show as having focal deletions in cells captured at their later replicating stage; these regions would have not started to duplicate by the time the sample was prepared for sequencing. These scattered patterns Supplementary Fig. 2 do not directly reflect the evolutionary history of the cells and are detrimental to phylogenetic tree inference.

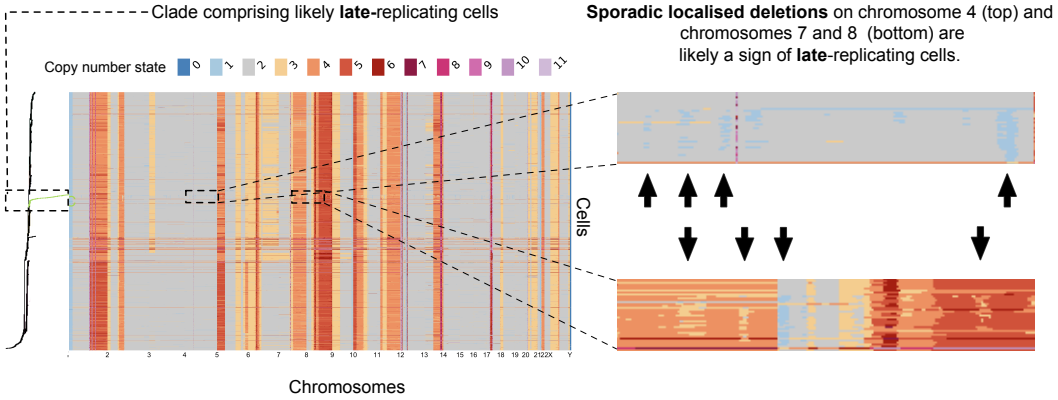

Supplementary Figure 2 – An example of replicating cells. Note the scattered localised deletions. This heatmap is from a HER2+ PDX line. These late replicating cells form a *finger* like clade in the tree. The top inset shows chromosome 4 while the bottom inset spans chromosomes 7 and 8.

Here we rank cells by the number of changes in their copy number states (a change is measured between consecutive bins) and pick the 90% percentile. The file `cn_bin_cell_filtered_no_jump.csv.gz` contains the integer copy number state with the final list of cells and genomic bins. An example input matrix is shown in Fig. 1-**a** where the integer copy numbers are coloured coded in a heatmap. Attrition rate due to filtering of cells is shown in Supplementary Table 2.

2. Baseline methods

Here we give a brief description of the baseline methods to which we compare sitka. `UPGMA` Sokal, 1958, `WPGMA` Sokal, 1958 and Neighbour Joining (NJ) Saitou and Nei, 1987 are all distance-based phylogenetic inference methods, that is, they use the input data to first compute a similarity matrix between single-cells and then proceed to construct an agglomerative clustering in an iterative process. HDBSCAN Campello et al., 2013 on the other hand is a heuristic that, roughly speaking, computes the minimum spanning tree from a low dimensional representation of the CN matrix. MEDALT Wang et al., 2021 is another distance based method that uses the Chu–Liu's algorithm to compute a directed minimum spanning tree from the matrix of minimum edit distance. Medicc2 Kaufmann et al., 2022 uses a finite state transducer to model copy number evolution over time, taking into account allele specific and whole genome duplication events. MrBayes Huelsenbeck and Ronquist, 2001 is a Bayesian phylogenetics framework that

implements multiple evolutionary models and uses MCMC to approximate the posterior distribution of trees and model parameters.

3. Tree shape statistics

All three trees from the three real data experiments are imbalanced Bortolussi et al., 2006 relative to a Yule model (Supplementary Fig. 3-**a**). Unbalanced tree topologies appear and are expected in adapting populations Neher and Hallatschek, 2013. In *SA*535 and *OV*2295 the sample subtrees become more balanced over time and post-relapse respectively. In contrast, *SA*501 exhibits a decrease in balancedness, except timepoint X11, where a marked increase in imbalance is observed (Supplementary Fig. 3-**b,c**).

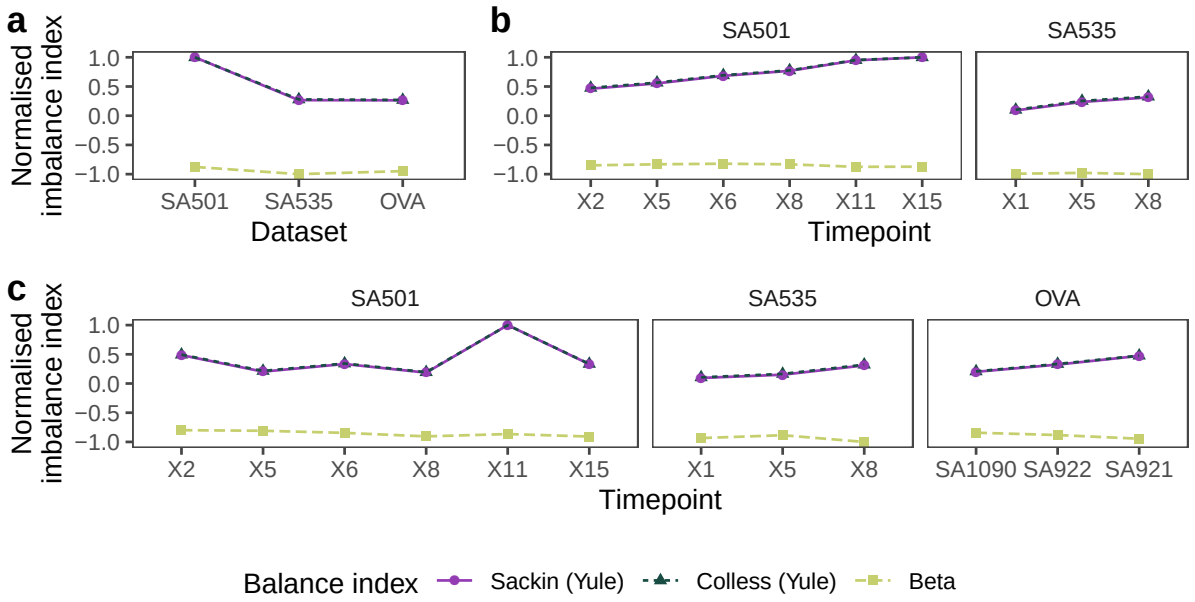

Supplementary Figure 3 – **(a)** Tree imbalance index where zero indicates that the tree is consistent with one simulated from a Yule model (completely balanced) and positive values indicate deviation from the Yule model (more imbalanced). For ease of plotting, each balance index is normalised by the absolute value of the maximum estimated statistic among all samples. Cumulatively adding more timepoints (**b**), or for the maximal subtree comprising cells of a specific timepoint (**c**).

sitka inferred trees are not dichotomous therefore we first resolve multichotomies into dichotomies. As there are multiple ways to resolve multichotomies, we do this 100 times, resolving multichotomies uniformly at random. We then compute the balance statistics on each resulting dichotomous tree and report the average in Supplementary Fig. 3-**a-c**. We report three balance statistics, namely Sackin, Colless, and Beta Paradis, 2011.

The Sackin Coronado et al., 2020 and Colless Coronado et al., 2020 statistics are both measures of imbalance of a rooted phylogenetic tree. The former is the sum of the depth of the leaves, while the latter is the sum of the absolute values of the difference between the number of descendent leaves of the left and the right child of each internal node. The Yule Coronado et al., 2020 model is a probabilistic model for bifurcating phylogenetic trees. Under this stochastic model, a phylogenetic tree with N leaves is generated by an iterative process: given rooted tree with 2 leaves, pick a leaf node uniformly randomly, and attach two new leaf nodes to it until the tree has N nodes.

We measure the change in the balance of the tree over time in two ways: (i) starting with the first timepoint and progressively adding more timepoints Supplementary Fig. 3-**b**), (ii) in individual timepoints Supplementary Fig. 3-**c**). In the former, we start with the maximal subtree $\tau_{\max}(X_{t_0})$ for cells in the first timepoint (X_{t_0}), then compute the maximal subtree that contains the

Dataset	parameter	value
Real datasets	`engine`	`PT`
Real datasets	`globalParameterization`	`true`
Real datasets	`fprBound`	0.1
Real datasets	`fnrBound`	0.5
Real datasets	`nChains`	1
Real datasets	`nScans`	1000
Real datasets	`nPassesPerScan`	1
Real datasets	`thinning`	1
Real datasets	`burnin fraction`	0.5
*S*90	`engine`	`PT`
*S*90	`globalParameterization`	`true`
*S*90	`fprBound`	0.5
*S*90	`fnrBound`	0.5
*S*90	`nChains`	1
*S*90	`nScans`	20000
*S*90	`nPassesPerScan`	1
*S*90	`thinning`	1
*S*90	`burnin fraction`	0.5
*S*10	`globalParameterization`	`true`, `false`
*S*130	`globalParameterization`	`true`
*S*10,*S*130	`engine`	`PT`
*S*10,*S*130	`fprBound`	0.1
*S*10,*S*130	`fnrBound`	0.5
*S*10,*S*130	`nChains`	8
*S*10,*S*130	`nScans`	5000
*S*10,*S*130	`nPassesPerScan`	10
*S*10,*S*130	`thinning`	1
*S*10,*S*130	`burnin fraction`	0.5

Supplemental Table 1 – Inference settings used for each dataset.

first two timepoints $\tau_{\max}((X_{t_0}, X_{t_1}))$, and continue until all timepoints are included. We report the imbalance statistic for each subtree constructed in this process. In the latter, for each timepoint X_t, we find the maximal subtree $\tau_{\max}(X_t)$ that contains all cells from timepoint X_t, and report the imbalance index for it.

index	dataset	sample.id	lib.id	tp	total	!mouse	qual.	!sphase	!lmr	final	finalr
1	SA501	SA501X2XB00096	A95621B	X2	623	570	524	580	568	498	498
2	SA501	SA501X2XB00097	A96171A	X2	492	36	21	474	37	20	20
3	SA501	SA501X2XB00097	A96109A	X2	656	59	37	399	96	34	34
4	SA501	SA501X5XB00877	A95670A	X5	615	326	253	575	252	238	228
5	SA501	SA501X6XB00294	A96213A	X6	1000	326	152	886	168	62	62
6	SA501	SA501X6XB00969	A95670B	X6	636	383	325	602	300	319	272
7	SA501	SA501X8XB01694	A90696ABC	X8	3672	3517	273	3482	1985	261	241
8	SA501	SA501X11XB00529	A96187A	X11	1063	1024	878	888	958	779	763
9	SA501	SA501X11XB00529	A96174A	X11	1234	1192	291	1007	258	116	58
10	SA501	SA501X15XB00929	A96173A	X15	1388	997	558	1131	667	399	399
11	TNBC-SA535	SA535X1XB00174	A96165B	X1	379	208	73	218	277	62	62
12	TNBC-SA535	SA535X5XB00517	A95732A	X5	928	613	372	776	464	332	324
13	TNBC-SA535	SA535X8XB00143	A95736A	X8	1072	410	194	956	354	154	152
14	OVA-2295	SA921	A90554A	TOV2295(R)	628	506	415	524	525	392	392
15	OVA-2295	SA922	A90554B	OV2295(R2)	596	466	303	518	467	296	296
16	OVA-2295	SA1090	A96213A	OV2295	1484	1438	1144	1092	1402	850	838

Supplemental Table 2 – Summary of real-world datasets used. `final` is the final number of cells after all filters except for `!lmr` are applied. `final` additionally filters out `lmr` cells, those that have total mapped reads fewer than 500,000. Abbreviations used are tp: time point; qual. : quality; !sphase: not sphase; !lmr: not low mapped reads.

https://doi.org/10.24072/pcjournal.292